



ELSEVIER



Available online at www.sciencedirect.com

ScienceDirect

Comput. Methods Appl. Mech. Engrg. 363 (2020) 112812

Computer methods
in applied
mechanics and
engineering

www.elsevier.com/locate/cma

Multi-material thermomechanical topology optimization with applications to additive manufacturing: Design of main composite part and its support structure

Oliver Giraldo-Londoño^a, Lucia Mirabella^b, Livio Dalloro^b, Glaucio H. Paulino^{a,*}

^a School of Civil and Environmental Engineering, Georgia Institute of Technology, 790 Atlantic Drive, Atlanta, GA 30332, USA

^b Siemens Corporate Technology, 755 College Road East, Princeton, NJ 08540, USA

Received 28 March 2019; received in revised form 20 December 2019; accepted 22 December 2019

Available online 24 February 2020

Abstract

This paper presents a density-based topology optimization formulation for the design of multi-material thermoelastic structures. The formulation is written in the form of a multi-objective topology optimization problem that considers two competing objective functions, one related to mechanical performance (mean compliance) and one related to thermal performance (either thermal compliance or temperature variance). To solve the optimization problem, we present an efficient design variable update scheme, which we have derived in the context of the Zhang–Paulino–Ramos (ZPR) update scheme by Zhang et al. (2018). The new update scheme has the ability to solve non-self-adjoint topology optimization problems with an arbitrary number of volume constraints, which can be imposed either to a subset of the candidate materials, or to sub-regions of the design domain, or to a combination of both. We present several examples that explore the ability of the formulation to obtain candidate Pareto fronts and to design support structures for additive manufacturing. Enabled by the ZPR update scheme, we are able to control the complexity and the length scale of the support structures by means of regional volume constraints. © 2019 Elsevier B.V. All rights reserved.

Keywords: Topology optimization; Multi-physics; Thermomechanical analysis; Additive manufacturing; Pareto front; ZPR update scheme

1. Introduction

Topology optimization has enjoyed vast success across different engineering fields, yet the majority of studies found in the literature have used this technique to solve single-physics problems. Numerical techniques that account for multiple physical phenomena are often required for the solution of complex industrial problems. Thus, to use topology optimization as a tool for the design of more complex engineering systems, it is fundamental to have a robust formulation capable of accounting for various physical phenomena.

The present study focuses on a subset of multi-physics topology optimization problems dealing with the design of multi-material structures subjected to thermomechanical loads. The formulation is presented in the form of a multi-objective topology optimization problem, such that the objective function is written as a weighted sum of a mechanical objective function (mechanical compliance) and a thermal objective function (either thermal compliance or temperature variance). The formulation also incorporates a general type of volume constraints that can be imposed to a subset of the candidate materials, to sub-regions of the design domain, or to a combination of the two (e.g., see [1,2]).

* Corresponding author.

E-mail address: paulino@gatech.edu (G.H. Paulino).

To update the design variables, we introduce a scheme that is designed to solve non-self-adjoint topology optimization problems with multiple constraints in an efficient manner. The new update scheme is an extension of the Zhang–Paulino–Ramos (ZPR) update scheme [1], with the main difference being the convex approximation of the objective function that we use to solve the subproblem at each optimization step. The new convex approximation is based on the concept of *sensitivity separation* recently introduced by Jiang et al. [3], in which the sensitivity of the objective function is expressed as the sum of a positive component and a negative component. We select the values of the positive and negative components of the sensitivity such that our convex approximation uses approximate second order information of the objective function.

The remainder of this paper is organized as follows. Section 2 provides the motivation for our work as well as a literature review on thermoelastic topology optimization. Section 3 introduces the multi-objective topology optimization formulation that we use for the design of multi-material thermoelastic structures. We elaborate on the new design variable update scheme in Section 4. In Section 5, we discuss two applications of interest using our topology optimization approach, i.e., the construction of candidate Pareto fronts and the design of support structures for additive manufacturing. We present several numerical examples in Section 6, followed by an assessment of computational efficiency in Section 7. We finalize the paper with several concluding remarks in Section 8.

2. Motivation and related work

Topology optimization provides an avenue to design complex structures that optimize a given performance measure. Given the nature of this computational technique, optimized structural topologies are often complex, and thus, their manufacturing may be challenging. The fabrication of optimized topologies is particularly challenging when the optimized topologies are composed of multiple material phases. However, recent advances in additive manufacturing technologies have enabled the fabrication of increasingly complex structures and material microstructures [4,5]. Moreover, recent studies have shown the feasibility of manufacturing single-material [6] and multi-material [1,2] structures obtained from topology optimization results.

The ability to design and manufacture multi-material structures enables designers to expand their design landscape, allowing them to conceive structures with increasing functionality. For instance, Qi and Halloran [7] manufactured topologically optimized bi-material microstructures with negative thermal expansion. More recently, Gaynor et al. [8] used PolyJet 3D printing to manufacture a bi-material compliant force inverter with increased performance (in terms of deflection), as compared to its single-material counterpart. By spatially tailoring the elastic properties of a material through several optimized microstructural configurations, Schumacher et al. [9] manufactured deformable parts, such that some regions of the part are stiff and some others are soft, allowing for enhanced functionality. Given the growing interest in additive manufacturing for multi-material structures, the number of publications pertaining topology optimization of such structures has recently increased. For a more comprehensive review of topology optimization for multi-material structures, we refer the interested readers to Zhang et al. [1] and Sanders et al. [2] and the references therein.

The aforementioned examples motivate the use of multi-material topology optimization to achieve structural designs with increased functionality. However, the applications of multi-material topology optimization found in the literature are mostly limited to designs in which a single physical phenomenon is considered (e.g., parts subjected only to mechanical forces or to temperature changes). In the present study, we are interested in the design of multi-material parts subjected to multiple physical phenomena. Particularly, we focus on the design of thermoelastic structures, i.e., structures subjected to both mechanical and thermal loads. We are interested in thermomechanical topology optimization problems because structures that operate in a thermal environment are subjected to temperature changes that may impact their performance, and as such, these effects must be accounted for in their design. We present a multi-material topology optimization formulation that is able to account for thermomechanical loads and implement it within the framework of PolyMat, a topology optimization code for compliance minimization of multi-material elastic structures written in Matlab [10].

One of the early studies in topology optimization of thermoelastic structures is that by Rodrigues and Fernandes [11]. They presented a topology optimization approach, based on homogenization theory, for the design of single-material structures subjected to thermal loads. In their formulation, the temperature distribution is assumed independent of the design variables (i.e., the temperature distribution is a prescribed quantity). Sigmund [12,13] introduced a topology optimization framework for the design of electro-thermo-mechanical micro actuators made of one or two materials. The design of these actuators considers the effects of geometric nonlinearities, an important

consideration for the design of these structural systems. Du et al. [14] used a mesh-free approach for the design of thermally driven compliant actuators. Similarly to Sigmund [12,13], their thermomechanical model considers geometric nonlinearities.

Sigmund and Torquato [15] and Sigmund and Torquato [16] presented a formulation for the topology optimization of a three-phase composite (two solid materials and void) with extreme thermal properties. They designed microstructures for maximized thermal expansion, zero thermal expansion, or negative thermal expansion, which highlight the potential functionality of multi-material designs. Another study concerning the design of materials and material systems subjected to thermomechanical effects is that by de Kruijf et al. [17]. They formulated the problem as a bi-objective topology optimization problem, such that the objective function is a linear combination of the bulk modulus and thermal conductivity. Their designs are made of two materials, one of them being stiff and less conductive and the other being compliant and more conductive.

Faure et al. [18] presented a level-set-based topology optimization approach for the design of multi-material microstructures with extreme thermal expansion (i.e., materials with minimal or maximal thermal expansion), considering gradation across material interfaces. Xia and Wang [19] used the level-set method for the compliance minimization of structures subjected to prescribed thermomechanical loads. In addition to the level-set method, the evolutionary structural optimization (ESO) method has been used for the design of thermoelastic structures under prescribed thermal loads [20], for non-uniform or for transient loads [21], and for the design of materials for heat conduction [22].

Topology optimization has also been used to solve thermomechanical problems with strength-related considerations. For instance, Takezawa et al. [23] conducted a study on topology optimization of thermoelastic structures with both stress and thermal conductivity constraints. The optimization statement is formulated as a volume minimization problem with constraints in von Mises stress and in thermal compliance, such that the local stress constraints are aggregated into a global constraint using a p -norm aggregation function. A similar study considering von Mises stress constraints is that by Deaton and Grandhi [24]. In their study, the local stress constraints were aggregated into m regional constraints using a p -norm aggregation function for each region. In the context of the level-set method, Deng and Suresh [25] investigated the stress-constrained topology optimization problem of thermoelastic structures using a global measure of stress also obtained via a p -norm aggregation function.

The studies discussed above focus on the design of single-scale structures. However, several studies have focused on the design of multi-scale structures, in which both the topology of the macro- and micro-structures are optimized. For instance, Yan et al. [26,27] presented an optimization technique for the concurrent optimization of macro- and micro-structures subjected to thermomechanical loads. Their approach is a direct extension of their previous work [28], which is related to the concurrent optimization of elastic structures. In the context of multi-objective topology optimization, Deng et al. [29] also introduced a multi-scale optimization approach to obtain structures that attain both minimum structural compliance and minimum thermal expansion.

Most studies related to thermomechanical topology optimization are able to yield single-material or two-material structures, which limits the possibility to achieve truly multifunctional designs. A step towards the design of multi-material thermoelastic structures is found in a study by Gao and Zhang [30]. In their study, they set the thermal stress coefficient of the material (i.e., the product of the Young's modulus and the thermal expansion coefficient) as a function of the element densities. The thermal stress coefficient is taken as a material property, and thus, its value for intermediate element densities can be interpolated using a single-material interpolation function, such as the Solid Isotropic Material with Penalization (SIMP), or a multi-material interpolation function, such as in the Discrete Material Optimization (DMO) method [31,32]. Their way of defining this thermomechanical material property allows them to simplify the topology optimization formulation and facilitates the implementation for multi-material structures. More recently, Gao et al. [33] extended their previous work [30] to the topology optimization of multi-material thermoelastic structures and use DMO interpolation scheme to find the effective thermomechanical properties (e.g., Young's modulus, thermal expansion coefficient, and thermal stress coefficient) for intermediate densities. The optimization statement is formulated as a compliance minimization problem with a mass constraint.

To the best of the authors' knowledge, we are still lacking a robust approach for the design of multi-material thermoelastic structures that considers multiple objective functions and a more general setting for volume constraints. Thus, the goal of this study is to put forth a multi-objective topology optimization approach with a flexible volume constraint setting, for the design of structures subjected to thermomechanical loads. Our work is an

extension of the studies by Zhang et al. [1], Sanders et al. [2], and Sanders et al. [10], which focus on single-physics topology optimization of multi-material structures.

Our approach considers two conflicting objective functions, one related to mechanical performance and one related to thermal performance. The mechanical performance is measured using the structural compliance of the system, while the thermal performance is measured by either one of two thermal objective functions: thermal compliance or temperature variance. The former thermal objective aims to find the structure with minimal mean temperature and the latter to find the structure with the most homogeneous temperature distribution. The choice of thermal objective function depends on the application of interest. The formulation also incorporates a general type of volume constraint, which can be imposed to a subset of candidate materials, to subregions of the design domain, or to a combination of the two [1,2]. To update the design variables, we present an extension of the design variable update scheme introduced by Jiang et al. [3], which we recast in the context of the ZPR scheme by Zhang et al. [1] for multi-material topology optimization. We present several examples, in which we use our formulation for the construction of candidate Pareto fronts and for the design of support structures for additive manufacturing.

The latter is an interesting application of topology optimization of thermoelastic structures, yet only a handful of studies have focused on this problem while considering thermomechanical effects (e.g., see Allaire and Bogosel [34]). A detailed literature survey on topology optimization for support structures can be found in their study as well as in studies by Allaire et al. [35] and by Mirzendehtel and Suresh [36]. In the study by Allaire and Bogosel [34], they use the level-set method to design support structures that conduct away heat produced during the additive manufacturing process. Similarly to the results we obtain, their methodology yields optimized support structures which are primarily composed of vertical struts. However, our optimized topologies contain branch-like features at the support locations, which are lacking in the results reported by Allaire and Bogosel [34].

3. Topology optimization formulation

This section presents the topology optimization formulation that we use for the design of thermomechanical structures. We begin by discussing the topology optimization statement, followed by a description of the thermo-mechanical boundary value problem that we solve to obtain both the temperature and displacement fields. Next, we discuss the material interpolation scheme used to obtain the effective thermomechanical material properties for intermediate element densities. Finally, we present the sensitivity analysis for the thermomechanical objective function.

3.1. Optimization statement

The optimization statement that we solve in the present study is

$$\begin{aligned}
 & \min_{\mathbf{z}_1, \dots, \mathbf{z}_m} J(\mathbf{z}_1, \dots, \mathbf{z}_m) = wJ_m + (1 - w)J_\theta \\
 & \text{s.t. } g_j = \frac{\sum_{i \in \mathcal{M}_j} \sum_{e \in \mathcal{E}_j} v_e \rho_i^e}{\sum_{e \in \mathcal{E}_j} v_e} - \bar{v}_j \leq 0, \quad j = 1, \dots, N_c \\
 & 0 < z_{\min} \leq z_i^e \leq 1, \quad e = 1, \dots, N_e, \quad i = 1, \dots, m \\
 & \text{with: } \mathbf{K}(\mathbf{z}_1, \dots, \mathbf{z}_m)\mathbf{u} = \mathbf{f} = \mathbf{f}_m + \mathbf{f}_{th} \\
 & \mathbf{H}(\mathbf{z}_1, \dots, \mathbf{z}_m)\boldsymbol{\theta} = \mathbf{f}_\theta \\
 & \boldsymbol{\rho}_i = \mathbf{P}\mathbf{z}_i, \quad i = 1, \dots, m
 \end{aligned} \tag{1}$$

where the objective function, $J(\mathbf{z}_1, \dots, \mathbf{z}_m)$, is defined in terms of a mechanical objective, J_m , and a thermal objective, J_θ , where $0 \leq w \leq 1$ is a weight factor. The design variables, $\mathbf{z}_1, \dots, \mathbf{z}_m$, correspond to vectors of element densities (one vector for each of the m candidate materials); g_j , $j = 1, \dots, N_c$ is the j th volume constraint, which can be imposed to a subset (\mathcal{M}_j) of the m candidate materials, to sub-regions of the design domain (\mathcal{E}_j), or to a combination of both [1,2]; v_e is the area of element e ; \bar{v}_j is the upper limit for volume constraint j ; $\mathbf{K}\mathbf{u} = \mathbf{f}$ is the linear elastic equilibrium equation, where \mathbf{K} , \mathbf{u} , and \mathbf{f} are the stiffness matrix, displacement vector, and load vector, respectively; $\mathbf{H}\boldsymbol{\theta} = \mathbf{f}_\theta$ is the linear system used to find the temperature distribution, where \mathbf{H} , $\boldsymbol{\theta}$, and \mathbf{f}_θ are the

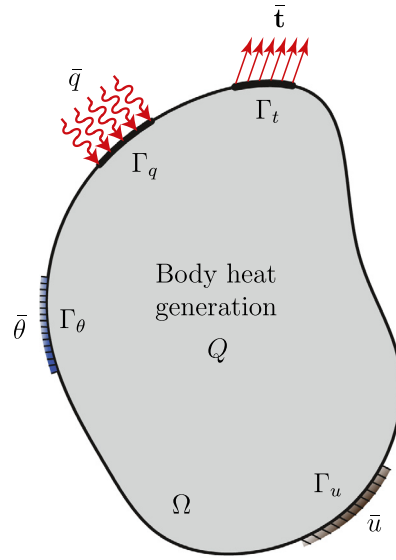


Fig. 1. Body subjected to mechanical and thermal loads.

conductivity matrix, nodal temperature vector, and thermal flux vector, respectively; and $\rho_i = \mathbf{Pz}_i$, $i = 1, \dots, m$ are vectors of filtered densities.

In this study, we use a linear filter [37], such that the filter matrix is given by

$$P_{ij} = \frac{w_{ij}v_j}{\sum_{k=1}^{N_e} w_{ik}v_k}, \quad \text{with } w_{ij} = \max \left[0, \left(1 - \frac{\|\mathbf{x}_i - \mathbf{x}_j\|_2}{R} \right) \right], \quad (2)$$

where R is the filter radius and $\|\mathbf{x}_i - \mathbf{x}_j\|_2$ is the distance between the centroids of elements i and j .

The thermal force vector for element e , \mathbf{f}_e^h , is computed as

$$\mathbf{f}_e^h = \beta_e \theta_e \bar{\mathbf{f}}_e^h, \quad \bar{\mathbf{f}}_e^h = \int_{\Omega_e} \mathbf{B}_e^T \phi d\Omega, \quad \phi = [1 \ 1 \ 0]^T, \quad (3)$$

where β_e is the effective thermal stress coefficient, θ_e is the temperature change evaluated at the centroid of the element, \mathbf{B}_e is the strain–displacement matrix. Similarly, the element thermal flux vector, \mathbf{f}_e^θ is obtained as

$$\mathbf{f}_e^\theta = \int_{\Omega_e} \mathbf{N}_e^T Q d\Omega - \int_{\partial\Omega_e} \mathbf{N}_e^T q dS, \quad (4)$$

where Q and q are the body heat generation and heat flux, respectively (see Fig. 1), and \mathbf{N}_e is the vector of shape functions for element e .

We use the mean compliance to assess the mechanical performance of the structure. That is the mechanical objective function, J_m , in optimization statement (1) is given by

$$J_m = \mathbf{u}^T \mathbf{K} \mathbf{u}. \quad (5)$$

In addition, we consider either of two thermal objective functions, J_θ , to assess the thermal performance of the structure. The first thermal objective function in (1) corresponds to the thermal compliance,

$$J_\theta = \boldsymbol{\theta}^T \mathbf{H} \boldsymbol{\theta} \quad (6)$$

and the second thermal objective function to the temperature variance,

$$J_\theta = \frac{1}{N_n} (\boldsymbol{\theta} - \mathbf{1}\theta_{avg})^T (\boldsymbol{\theta} - \mathbf{1}\theta_{avg}), \quad (7)$$

where $\theta_{avg} = \frac{1}{N_n} \mathbf{1}^T \boldsymbol{\theta}$ is the average temperature of the structure, N_n is the number of nodes in the FE mesh, $\boldsymbol{\theta}$ is the vector of nodal temperatures, and $\mathbf{1}$ is a vector with unit entries. The first thermal objective aims to find

the structure with the least overall temperature, which indirectly helps to reduce thermal stresses, and the second thermal objective aims to find the structure with the most homogeneous temperature distribution, which reduces thermal warping.

3.2. Thermomechanical boundary value problem

Consider a body subjected to mechanical and thermal loads shown in Fig. 1. We obtain both the displacement field, \mathbf{u} , and the temperature field, θ , by solving a weakly coupled thermomechanical boundary value problem. To find the temperature field, θ , we solve the thermal boundary value problem (BVP)

$$\begin{aligned} -q_{j,j} + Q &= 0, & \text{in } \Omega \\ q_j &= -\kappa\theta_{,j}, & \text{in } \Omega \\ \theta &= \bar{\theta}, & \text{on } \Gamma_\theta \\ q_j n_j &= \bar{q}, & \text{on } \Gamma_q \end{aligned} \tag{8}$$

where q_j is the heat flux vector, Q is the body heat generation, κ is the thermal conductivity, $\bar{\theta}$ is the temperature prescribed on boundary Γ_θ , and \bar{q} is the heat flux prescribed on boundary Γ_q .

The temperature field obtained from the solution of BVP (8) is used to find the displacement field, \mathbf{u} , by solving the following BVP:

$$\begin{aligned} \sigma_{ij,j} + b_j &= 0, & \text{in } \Omega \\ \sigma_{ij} &= E_{ijkl}(\varepsilon_{kl} - \alpha\theta\delta_{kl}), & \text{in } \Omega \\ \varepsilon_{ij} &= \frac{1}{2}(u_{i,j} + u_{j,i}), & \text{in } \Omega, \\ u_j &= \bar{u}_j, & \text{on } \Gamma_u \\ \sigma_{ij} n_j &= \bar{t}_j, & \text{on } \Gamma_t \end{aligned} \tag{9}$$

where σ_{ij} is the stress tensor, b_j is the body force vector, E_{ijkl} is the elasticity tensor, ε_{ij} is the strain tensor, α is the thermal expansion coefficient, θ is the relative temperature, δ_{kl} is the Kronecker delta operator, \bar{u}_j are prescribed displacements applied on boundary Γ_u , and \bar{t}_j are prescribed traction applied on boundary Γ_t . Note that, in the boundary value problems (8)–(9), the temperature field θ affects the displacement field \mathbf{u} , but the displacement field has no effect on the temperature field.

3.3. Material interpolation

Given that the optimization statement (1) considers an arbitrary number of candidate materials, m , it is essential that we use an appropriate material interpolation scheme to find the effective thermal and mechanical properties for intermediate values of element densities. In the present study, we use the modified version of the DMO interpolation scheme [31,32] introduced by Sanders et al. [10]. The DMO interpolation scheme was proposed for the design of layered composites, but has been used as an extension of the SIMP interpolation scheme [38,39] for the design of multi-material structures using density-based topology optimization.

Based on the modification introduced by Sanders et al. [10], we find the effective thermomechanical properties for an element e of the FE mesh as follows:

$$\begin{aligned} E_e(\rho_1^e, \dots, \rho_m^e) &= \varepsilon_E + (1 - \varepsilon_E) \sum_{i=1}^m w_i^e \prod_{\substack{j=1 \\ j \neq i}}^m (1 - \gamma w_j^e) E_i^0, \\ \beta_e(\rho_1^e, \dots, \rho_m^e) &= \varepsilon_\beta + (1 - \varepsilon_\beta) \sum_{i=1}^m w_i^e \prod_{\substack{j=1 \\ j \neq i}}^m (1 - \gamma w_j^e) \beta_i^0, \quad \text{and} \\ \kappa_e(\rho_1^e, \dots, \rho_m^e) &= \varepsilon_\kappa + (1 - \varepsilon_\kappa) \sum_{i=1}^m w_i^e \prod_{\substack{j=1 \\ j \neq i}}^m (1 - \gamma w_j^e) \kappa_i^0, \end{aligned} \tag{10}$$

where

$$w_i^e = (\rho_i^e)^p \quad \text{and} \quad w_i^e = \frac{\rho_i^e}{1 + q(1 - \rho_i^e)}, \tag{11}$$

for the SIMP and RAMP models, respectively. In Eqs. (10), E_e , β_e , and κ_e correspond to the effective Young’s modulus, thermal stress coefficient, and thermal conduction, respectively; E_i^0 , β_i^0 , and κ_i^0 , to the Young’s modulus, thermal stress coefficient, and thermal conduction of candidate material i , $i = 1, \dots, m$; and ε_E , ε_β , and ε_κ to their corresponding Ersatz-like parameters. The thermal stress coefficient β_i^0 for material i is defined as the product of the Young’s modulus E_i^0 and the thermal expansion coefficient, α_i^0 , i.e., $\beta_i^0 = \alpha_i^0 E_i^0$. Parameter γ ($0 \leq \gamma \leq 1$) in Eqs. (10) is a mixing penalty parameter, which for compliance minimization problems leads to a convex formulation with no penalization on material mixing when $p = 1$ and $\gamma = 0$ and to a non-convex formulation with full penalization on material mixing when $p \geq 1$ and $\gamma = 1$. We use a continuation on both parameters p and γ [10], which is analogous to the continuation in the penalty parameter p typically used in single-material topology optimization.

3.4. Sensitivity analysis

The sensitivity of the objective function, $J(\mathbf{z}_1, \dots, \mathbf{z}_m)$, with respect to the design variables, \mathbf{z}_i , $i = 1, \dots, m$, is obtained using the chain rule as follows:

$$\frac{\partial J}{\partial \mathbf{z}_i} = \frac{\partial \rho_i}{\partial \mathbf{z}_i} \left(\frac{\partial \mathbf{E}}{\partial \rho_i} \frac{\partial J}{\partial \mathbf{E}} + \frac{\partial \boldsymbol{\beta}}{\partial \rho_i} \frac{\partial J}{\partial \boldsymbol{\beta}} + \frac{\partial \boldsymbol{\kappa}}{\partial \rho_i} \frac{\partial J}{\partial \boldsymbol{\kappa}} \right), \tag{12}$$

where $\mathbf{E} = [E_1, \dots, E_{N_e}]^T$, $\boldsymbol{\beta} = [\beta_1, \dots, \beta_{N_e}]^T$, and $\boldsymbol{\kappa} = [\kappa_1, \dots, \kappa_{N_e}]^T$. The first term on the right hand side of Eq. (12) is equal to the transpose of the filter matrix, \mathbf{P} , i.e., $\frac{\partial \rho_i}{\partial \mathbf{z}_i} = \mathbf{P}^T$. Moreover, the partial derivatives of the Young’s modulus, thermal stress coefficient, and thermal conductivity are obtained from Eqs. (10)–(11) as follows:

$$\frac{\partial \mathbf{E}}{\partial \rho_i} = \frac{\partial \mathbf{w}_i}{\partial \rho_i} \frac{\partial \mathbf{E}}{\partial \mathbf{w}_i}, \quad \frac{\partial \boldsymbol{\beta}}{\partial \rho_i} = \frac{\partial \mathbf{w}_i}{\partial \rho_i} \frac{\partial \boldsymbol{\beta}}{\partial \mathbf{w}_i}, \quad \text{and} \quad \frac{\partial \boldsymbol{\kappa}}{\partial \rho_i} = \frac{\partial \mathbf{w}_i}{\partial \rho_i} \frac{\partial \boldsymbol{\kappa}}{\partial \mathbf{w}_i}, \tag{13}$$

where

$$\frac{\partial w_i^k}{\partial \rho_i^\ell} = p(\rho_i^k)^{p-1} \delta_{k\ell} \quad \text{or} \quad \frac{\partial w_i^k}{\partial \rho_i^\ell} = \frac{1 + q}{[1 + q(1 - \rho_i^k)]^2} \delta_{k\ell} \tag{14}$$

for the SIMP and RAMP models, respectively, and

$$\begin{aligned} \frac{\partial E_k}{\partial w_i^\ell} &= (1 - \varepsilon_E) \left\{ \prod_{\substack{j=1 \\ j \neq i}}^m (1 - \gamma w_j^\ell) E_i^0 - \gamma \sum_{\substack{p=1 \\ p \neq i}}^m w_p^\ell \prod_{\substack{r=1 \\ r \neq p \\ r \neq i}}^m (1 - \gamma w_r^\ell) E_p^0 \right\} \delta_{k\ell}, \\ \frac{\partial \beta_k}{\partial w_i^\ell} &= (1 - \varepsilon_\beta) \left\{ \prod_{\substack{j=1 \\ j \neq i}}^m (1 - \gamma w_j^\ell) \beta_i^0 - \gamma \sum_{\substack{p=1 \\ p \neq i}}^m w_p^\ell \prod_{\substack{r=1 \\ r \neq p \\ r \neq i}}^m (1 - \gamma w_r^\ell) \beta_p^0 \right\} \delta_{k\ell}, \quad \text{and} \\ \frac{\partial \kappa_k}{\partial w_i^\ell} &= (1 - \varepsilon_\kappa) \left\{ \prod_{\substack{j=1 \\ j \neq i}}^m (1 - \gamma w_j^\ell) \kappa_i^0 - \gamma \sum_{\substack{p=1 \\ p \neq i}}^m w_p^\ell \prod_{\substack{r=1 \\ r \neq p \\ r \neq i}}^m (1 - \gamma w_r^\ell) \kappa_p^0 \right\} \delta_{k\ell}. \end{aligned} \tag{15}$$

The terms $\delta_{k\ell}$ above refer to the Kronecker delta operator.

The last terms needed to compute the sensitivity of the objective function are the partial derivatives of the objective with respect to the effective thermoelastic properties. These derivatives are obtained as

$$\begin{aligned} \frac{\partial J}{\partial \mathbf{E}} &= w \frac{\partial J_m}{\partial \mathbf{E}} + (1 - w) \frac{\partial J_\theta}{\partial \mathbf{E}}, \\ \frac{\partial J}{\partial \boldsymbol{\beta}} &= w \frac{\partial J_m}{\partial \boldsymbol{\beta}} + (1 - w) \frac{\partial J_\theta}{\partial \boldsymbol{\beta}}, \quad \text{and} \\ \frac{\partial J}{\partial \boldsymbol{\kappa}} &= w \frac{\partial J_m}{\partial \boldsymbol{\kappa}} + (1 - w) \frac{\partial J_\theta}{\partial \boldsymbol{\kappa}}. \end{aligned} \tag{16}$$

The derivatives of the mechanical objective, J_m , with respect to the effective thermoelastic properties are computed from Eq. (5) as

$$\begin{aligned} \frac{\partial J_m}{\partial E_e} &= -\mathbf{u}_e^T \frac{\partial \mathbf{K}_e}{\partial E_e} \mathbf{u}_e, \\ \frac{\partial J_m}{\partial \beta_e} &= 2\mathbf{u}_e^T \frac{\partial \mathbf{f}_e^{th}}{\partial \beta_e} = 2\theta_e \mathbf{u}_e^T \bar{\mathbf{f}}_e^{th}, \quad \text{and} \\ \frac{\partial J_m}{\partial \kappa_e} &= 0. \end{aligned} \tag{17}$$

We obtain the derivatives of each of the thermal objective functions, J_θ , with respect to the effective thermomechanical properties using Eqs. (6) or (7). For the thermal compliance, we use Eq. (6) and obtain

$$\frac{\partial J_\theta}{\partial E_e} = 0, \quad \frac{\partial J_\theta}{\partial \beta_e} = 0, \quad \text{and} \quad \frac{\partial J_\theta}{\partial \kappa_e} = -\boldsymbol{\theta}_e^T \frac{\partial \mathbf{H}_e}{\partial \kappa_e} \boldsymbol{\theta}_e. \tag{18}$$

Similarly, for the temperature variance, we use Eq. (7) and the adjoint method to obtain

$$\frac{\partial J_\theta}{\partial E_e} = 0, \quad \frac{\partial J_\theta}{\partial \beta_e} = 0, \quad \text{and} \quad \frac{\partial J_\theta}{\partial \kappa_e} = -\boldsymbol{\lambda}_e^T \frac{\partial \mathbf{H}_e}{\partial \kappa_e} \boldsymbol{\theta}_e, \tag{19}$$

where $\boldsymbol{\lambda}$ is the solution to the adjoint problem

$$\mathbf{H}\boldsymbol{\lambda} = \frac{2}{N_n} \left(\mathbf{I} - \frac{1}{N_n} \mathbf{1}\mathbf{1}^T \right) (\boldsymbol{\theta} - \mathbf{1}\theta_{avg}). \tag{20}$$

4. Design variable update

Given the increasing complexity of the topology optimization problems that are being solved nowadays, it is fundamental to have an efficient and robust design variable update scheme that can handle multiple constraints and materials and that is scalable to solve large-scale optimization problems. A suitable scheme for that purpose is the ZPR design variable update [1], yet this scheme is only designed to solve self-adjoint problems. However, the type of optimization problems that we intend to solve are typically non-self-adjoint.

To solve non-self-adjoint topology optimization problems with multiple materials and constraints, we extend the ZPR update scheme to allow for both positive and negative sensitivity values. To this end, we exploit ideas from the Convex Linearization method (CONLIN) [40,41] and the MMA family [42,43], in which the positive and negative components of the objective gradient are treated separately. In this study, we approximate the objective function, $J(\mathbf{z}_1, \dots, \mathbf{z}_m)$, at optimization step $k + 1$, with a non-monotonous convex approximation, $\tilde{J}(\mathbf{z}_1, \dots, \mathbf{z}_m)$, of the form:

$$\tilde{J}(\mathbf{z}_1, \dots, \mathbf{z}_m) = J(\mathbf{z}_1^k, \dots, \mathbf{z}_m^k) + \sum_{i=1}^m \{ \mathbf{a}_i^T [\mathbf{y}_i(\mathbf{z}_i) - \mathbf{y}_i(\mathbf{z}_i^k)] + \mathbf{b}_i^T (\mathbf{z}_i - \mathbf{z}_i^k) \}, \tag{21}$$

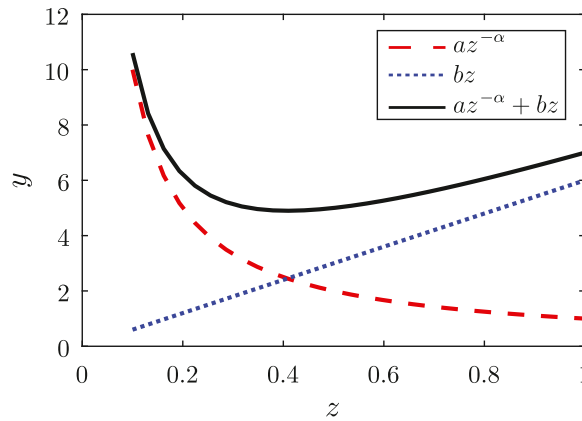


Fig. 2. Components of the non-monotonous linearization for a one-dimensional function.

where:

$$\begin{aligned}
 & \mathbf{y}_i(\mathbf{z}_i) = \mathbf{z}_i^{-\alpha}, \quad i = 1 \dots m, \quad \alpha > 0, \\
 & a_i^e = \frac{\partial J^-}{\partial y_i^e}(\mathbf{z}_1^k, \dots, \mathbf{z}_m^k) = -\frac{1}{\alpha} \left(z_i^{e,k} \right)^{1+\alpha} \frac{\partial J^-}{\partial z_i^e}(\mathbf{z}_1^k, \dots, \mathbf{z}_m^k) \geq 0, \quad e = 1, \dots, N_e, \\
 & b_i^e = \frac{\partial J^+}{\partial z_i^e}(\mathbf{z}_1^k, \dots, \mathbf{z}_m^k) \geq 0, \quad e = 1, \dots, N_e, \\
 & \frac{\partial J}{\partial z_i^e} = \frac{\partial J^+}{\partial z_i^e} + \frac{\partial J^-}{\partial z_i^e}
 \end{aligned} \tag{22}$$

The process of approximating the objective function, $J(\mathbf{z}_1, \dots, \mathbf{z}_m)$, with the convex approximation (21) is referred to as *sensitivity separation* [3]. The term sensitivity separation is used because the sensitivity of the objective function, $\partial J/\partial z_i^e$, is separated into a positive and a negative component, $\partial J^+/\partial z_i^e$ and $\partial J^-/\partial z_i^e$, respectively, such that $\partial J/\partial z_i^e = \partial J^+/\partial z_i^e + \partial J^-/\partial z_i^e$. To illustrate this point, Fig. 2 shows both components of the non-monotonous approximation (21) for a one-dimensional function.

The only requirement for the sensitivity separation to be well-defined is that $\partial J^+/\partial z_i^e \geq 0$ and that $\partial J^-/\partial z_i^e \leq 0$. As a result, we can define these positive and negative components in an infinite number of ways. For instance, Jiang et al. [3] separate the positive and negative components of the sensitivity as

$$\frac{\partial J^-}{\partial z_i^e} = \begin{cases} (1 + \bar{\beta}) \frac{\partial J}{\partial z_i^e} & \text{if } \frac{\partial J}{\partial z_i^e} \leq 0 \\ -\bar{\beta} \frac{\partial J}{\partial z_i^e} & \text{otherwise,} \end{cases} \quad \frac{\partial J^+}{\partial z_i^e} = \begin{cases} -\bar{\beta} \frac{\partial J}{\partial z_i^e} & \text{if } \frac{\partial J}{\partial z_i^e} \leq 0 \\ (1 + \bar{\beta}) \frac{\partial J}{\partial z_i^e} & \text{otherwise,} \end{cases} \tag{23}$$

where $\bar{\beta} > 0$ is a parameter that is tuned to control the aggressiveness of the design variable update. In the present study, we separate the positive and negative components of the sensitivity such that the curvature of the convex approximation, $\tilde{J}(\mathbf{z}_1, \dots, \mathbf{z}_m)$, is close to the curvature of the objective function, $J(\mathbf{z}_1, \dots, \mathbf{z}_m)$. We choose this way of separating the sensitivity to improve the convergence characteristics of the design variable update scheme.

The second-order derivatives of the convex approximation (21) at iteration k of the optimization process is given by

$$\frac{\partial^2 \tilde{J}}{\partial (z_i^e)^2} = a_i^e \alpha (\alpha + 1) (z_i^{e,k})^{-(\alpha+2)} \tag{24}$$

Substituting Eq. (22)₂ into Eq. (24) and solving for $\partial J^-/\partial z_i^e$ yields

$$\frac{\partial J^-}{\partial z_i^e} = \frac{\partial^2 \tilde{J}}{\partial (z_i^{e,k})^2} \frac{z_i^e}{\alpha + 1} \tag{25}$$

We use Eq. (25) to define the negative and positive components of the sensitivity as

$$\frac{\partial J^-}{\partial z_i^e} = \min \left\{ -\frac{|h_i^{e,k}| z_i^{e,k}}{\alpha + 1}, \frac{\partial J}{\partial z_i^e} \right\}, \quad \frac{\partial J^+}{\partial z_i^e} = \frac{\partial J}{\partial z_i^e} - \frac{\partial J^-}{\partial z_i^e}, \tag{26}$$

where $h_i^{e,k}$ are estimates of the second-order derivatives of the objective function at iteration k . To obtain Eqs. (26), we substitute $\frac{\partial^2 J}{\partial (z_i^e)^2} = |h_i^{e,k}|$ into Eq. (25) and impose constraints to the positive and negative components of the sensitivity, such that $\partial J^+ / \partial z_i^e \geq 0$ and $\partial J^- / \partial z_i^e \leq 0$.

Computing the second-order sensitivity information of the objective function is a computationally expensive proposition. For that reason, we only use an estimate of the second order derivatives, $h_i^{e,k}$, which we obtain based on variable metric algorithms such as BFGS [44–47]. Because $h_i^{e,k} \approx \partial^2 J / \partial (z_i^{e,k})^2$, we only need to approximate the diagonal of the Hessian matrix, which requires significantly less memory as compared to storing the full Hessian matrix. An approximation of the full Hessian matrix using the BFGS method is given by

$$\mathbf{B}_k = \mathbf{B}_{k-1} + \frac{\mathbf{c}_{k-1} \mathbf{c}_{k-1}^T}{\mathbf{c}_{k-1}^T \mathbf{s}_{k-1}} - \frac{\mathbf{B}_{k-1} \mathbf{s}_{k-1} \mathbf{s}_{k-1}^T \mathbf{B}_{k-1}}{\mathbf{s}_{k-1}^T \mathbf{B}_{k-1} \mathbf{s}_{k-1}} \tag{27}$$

where:

$$c_k = \left. \frac{\partial J}{\partial \mathbf{z}} \right|_{\mathbf{z}=\mathbf{z}^k} - \left. \frac{\partial J}{\partial \mathbf{z}} \right|_{\mathbf{z}=\mathbf{z}^{k-1}}, \quad s_k = \mathbf{z}^k - \mathbf{z}^{k-1}, \quad \text{and} \quad \mathbf{z} = [z_1^1, \dots, z_1^{N_e}, \dots, z_m^1, \dots, z_m^{N_e}]^T. \tag{28}$$

An approximate way of obtaining the diagonal components of the Hessian matrix from Eq. (27), which works for diagonally dominant Hessian matrices, consists of ignoring the off-diagonal terms of \mathbf{B}_k and \mathbf{B}_{k-1} . If these terms are ignored in Eq. (27), we can obtain an approximation of the diagonal of the Hessian matrix, $h_i^{e,k}$, as follows:

$$h_i^{e,k} = h_i^{e,k-1} + \frac{(c_i^{k-1})^2}{\mathbf{c}_{k-1}^T \mathbf{s}_{k-1}} - \frac{(h_i^{e,k-1})^2 (s_i^{k-1})^2}{\mathbf{h}_{k-1}^T \mathbf{s}_{k-1}^2}, \tag{29}$$

where $\mathbf{h}_{k-1} = [h_1^{1,k-1}, \dots, h_1^{N_e,k-1}, \dots, h_m^{1,k-1}, \dots, h_m^{N_e,k-1}]^T$.

We use the sensitivity separation technique described above to develop a design variable update, similar to the ZPR update, that can be used to solve topology optimization problems for non-self-adjoint problems with multiple materials and volume constraints. Using the approximate objective function (21), we can now define an approximate subproblem (neglecting the constant terms in Eq. (21)) as follows:

$$\begin{aligned} \min_{\mathbf{z}_1, \dots, \mathbf{z}_m} \quad & \tilde{J}(\mathbf{z}_1, \dots, \mathbf{z}_m) = \sum_{i=1}^m [\mathbf{a}_i^T \mathbf{y}_i(\mathbf{z}_i) + \mathbf{b}_i^T \mathbf{z}_i] \\ \text{s.t.} \quad & g_j(\mathbf{z}_1, \dots, \mathbf{z}_m) = g_j(\mathbf{z}_1^k, \dots, \mathbf{z}_m^k) + \sum_{i \in \mathcal{M}_j} \sum_{e \in \mathcal{E}_j} \frac{\partial g_j}{\partial z_i^e} (z_i^e - z_i^{e,k}) \leq 0, \quad j = 1, \dots, N_c \\ & z_{i,L}^{e,k} \leq z_i^e \leq z_{i,U}^{e,k}, \quad e = 1, \dots, N_e, \quad i = 1, \dots, m \end{aligned} \tag{30}$$

where

$$z_{i,L}^{e,k} = \max(z_{\min}, z_i^{e,k} - \text{move}) \quad \text{and} \quad z_{i,U}^{e,k} = \min(1, z_i^{e,k} + \text{move}). \tag{31}$$

The term “move” shown above refers to the move limit.

We write the Lagrangian of the approximate primal sub-problem (30) using Lagrange multipliers λ_j , $j = 1, \dots, N_c$, as shown below:

$$\begin{aligned} \mathcal{L}(\mathbf{z}_1, \dots, \mathbf{z}_m, \lambda_1, \dots, \lambda_{N_c}) &= \sum_{i=1}^m (\mathbf{a}_i^T \mathbf{y}_i + \mathbf{b}_i^T \mathbf{z}_i) + \sum_{j=1}^{N_c} \lambda_j g_j \\ &= \sum_{j=1}^{N_c} \left\{ \sum_{i \in \mathcal{M}_j} \sum_{e \in \mathcal{E}_j} \left[a_i^e y_i^e + b_i^e z_i^e + \lambda_j \frac{\partial g_j}{\partial z_i^e} (z_i^e - z_i^{e,k}) \right] + \lambda_j g_j(\mathbf{z}_1^k, \dots, \mathbf{z}_m^k) \right\} \end{aligned} \tag{32}$$

Writing the Lagrangian in the form shown above is possible only if the constraints g_j are such that each design variable z_i^e is associated with one constraint only. Note that the Lagrangian function shown has been written in

a separable form as $\mathcal{L} = \sum_{j=1}^{N_c} \mathcal{L}^{(j)}$. Given that the Lagrangian is separable, the minimizer of each $\mathcal{L}^{(j)}$ can be obtained independently, which leads to an update of the design variables written as

$$z_i^e(\lambda_j) = \begin{cases} z_{i,L}^e, & \text{if } B_i^e(\lambda_j) \leq z_{i,L}^{e,k} \\ B_i^e(\lambda_j), & \text{if } z_{i,L}^{e,k} < B_i^e(\lambda_j) \leq z_{i,U}^{e,k} \\ z_{i,U}^e, & \text{if } B_i^e(\lambda_j) \geq z_{i,U}^{e,k} \end{cases} \quad (33)$$

where

$$B_i^e(\lambda_j) = z_{i,L}^{e,k} \left[\frac{-\frac{\partial J^-}{\partial z_i^e}(\mathbf{z}_1^k, \dots, \mathbf{z}_m^k)}{\frac{\partial J^+}{\partial z_i^e}(\mathbf{z}_1^k, \dots, \mathbf{z}_m^k) + \lambda_j \frac{\partial g_j}{\partial z_i^e}(\mathbf{z}_1^k, \dots, \mathbf{z}_m^k)} \right]^{1+\alpha} \quad (34)$$

From the expression above, it is apparent that the update of each design variable depends only on the Lagrange multiplier of the constraint to which it is associated. Due to this attribute, the update of the design variables can easily be conducted in parallel, which makes this design variable update scheme attractive to solve large-scale topology optimization problems. Similar attributes were observed by Zhang et al. [1]; Sanders et al. [2] for the ZPR update scheme. The Lagrange multipliers λ_j in Eq. (34) are obtained by solving the stationary conditions of the dual problem associated to the primal approximate sub-problem (30). Similar to the procedure by Zhang et al. [1] or Sanders et al. [2], the Lagrange multipliers are found by solving

$$g_j(\mathbf{z}_1^k, \dots, \mathbf{z}_m^k) + \sum_{i \in \mathcal{M}_j} \frac{\partial g_j}{\partial \mathbf{z}_i}(\mathbf{z}_1^k, \dots, \mathbf{z}_m^k)^T (\mathbf{z}_i(\lambda_j) - \mathbf{z}_i^k) = 0, \quad (35)$$

which, due to its monotonic behavior, can easily be solved using any interval reducing method, e.g., bisection. Note that if we set $\partial J^+/\partial z_i^e = 0$ and $\partial J^-/\partial z_i^e = \partial J/\partial z_i^e$ in Eq. (34), the proposed update scheme reduces to the original ZPR update scheme [1,2]. In contrast to the ZPR update scheme, the proposed approach can be used to solve optimization problems that are either self-adjoint or non-self-adjoint. In addition, the proposed update scheme shares some of the attributes of the ZPR scheme in the sense that the update of design variables has similar computational cost as that of the OC update scheme [48,49].

In order to improve the robustness of the update scheme, we use a damping scheme, such that the design variables at iteration k are computed as

$$\mathbf{z}_i^k = \eta \mathbf{z}_i^k + (1 - \eta) \mathbf{z}_i^{k-1}, \quad i = 1, \dots, m, \quad (36)$$

where $0 < \eta < 1$ is a damping parameter, and \mathbf{z}_i^k and \mathbf{z}_i^{k-1} are the vectors of design variables at optimization steps k and $k - 1$, respectively. This damping scheme helps to reduce undesired oscillations in the design variables, which may happen when the approximation of the diagonal of the Hessian matrix is not accurate enough.

5. Some practical applications

The formulation that we have previously discussed can be used to solve a variety of topology optimization problems. Here, we focus on two potential applications of the present formulation: the construction of candidate Pareto fronts and the design of thermomechanical support structures for additive manufacturing.

5.1. Construction of candidate Pareto fronts

We construct candidate Pareto fronts by solving the optimization statement (1) for various values of $w = w_k$, $k = 1, \dots, n$, such that $w_1 = 0$ and $w_n = 1$. From our numerical solutions, we observed that the value of J_m^* becomes large when $w \rightarrow 0$ and the value of J_θ^* becomes large when $w \rightarrow 1$, which causes the points along the candidate Pareto front to be excessively spread when the values of w_k are equally spaced close to $w = 0$ or $w = 1$. To obtain a more even distribution of points across the candidate Pareto front, we sample the values of w_k in a non-uniform way, as follows:

$$w_k = \frac{1}{2} \left[1 + \cos \left(\frac{n-k}{n-1} \pi \right) \right], \quad k = 1, \dots, n. \quad (37)$$

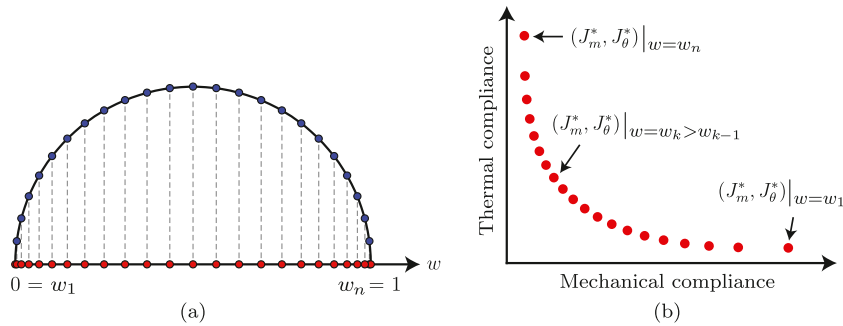


Fig. 3. Methodology for the construction of candidate Pareto fronts. A nonuniform set of weight factors w_k (a) is used to solve the optimization statement (1). The optimized values, $J_{m,k}^*$ and $J_{\theta,k}^*$ are plotted to construct the front (b) for the thermomechanical topology optimization problem.

An example of such point distribution is shown by the points on the w -axis in Fig. 3a and a schematic of a candidate Pareto front is shown in Fig. 3b. The points on the w -axis in Fig. 3a are obtained by projecting a set of points that are uniformly distributed along a semi-circle of diameter equal to one and center in $w = 0.5$.

A candidate Pareto front obtained using the framework described above provides a set of designs that designers can use when conceiving thermomechanical structures. The designer can select an efficient design from the candidate Pareto front depending on the desired level of importance between thermal and mechanical performance.

5.2. Design of support structures for additive manufacturing

The topology optimization statement (1) is also used to design support structures for additive manufacturing (AM) that are both structurally and thermally optimized. The framework for the design of support structures for AM is briefly outlined in Fig. 4. We start with an initial design domain with given applied loads (Fig. 4a), which can be either mechanical, thermal, or a combination of the two. For a given value of $w \in [0, 1]$, which depends on design considerations, we use the optimization statement (1) to obtain an optimized structure (Fig. 4b), which we refer to as the *primary structure*. Once the primary structure is designed, we define the orientation, ϕ , that we will use to print it and then proceed to rotate it. The rotated structure is projected onto a secondary mesh, which we refer to as the AM mesh, and use it for the design of the support structure (Fig. 4c). We consider the projected structure as a passive region in the AM mesh. To define the AM design problem, we impose a zero displacement boundary condition and a prescribed temperature of magnitude $\bar{\theta}$ to the bottom of the AM mesh, to represent the build plate. Finally, we use optimization statement (1) with a different value of w to design the support structure (Fig. 4d).

To design the support structure, we apply thermomechanical loads that resemble, in an approximate way, those obtained from the additive manufacturing process. As shown in Fig. 5, a surface traction, $\bar{\mathbf{t}}$, and a heat flux, \bar{q} , are applied to the model, but only to regions of the design domain that need support material. By only loading the nodes that need support material, we encourage material to appear in those regions. The regions that need support are identified using an overhang detection algorithm, which finds the parts of the boundary of the primary structure whose overhang angle, α , is larger than the critical overhang angle, α_c . As indicated in Fig. 5, we compute the overhang angles, α , based on the unit normal vectors to the boundary of the structure.

The applied surface traction, $\bar{\mathbf{t}}$, is used to represent the weight of the primary structure and can be computed from the nodal loads coming from body forces due to gravity. However, because we only load the nodes that need to be supported, we impose the nodal loads based on an approximate weight of the primary structure. Specifically, the magnitude of the nodal forces that we impose is equal to the approximate weight of the structure divided by the number of nodes that need to be supported. Moreover, the applied heat flux, \bar{q} , is used to represent the heat being transmitted to the support structure during the AM process. In order to mimic the changes in temperature through height that occur during 3D printing, we impose a non-uniform heat flux that varies with the height, as measured from the build plate. In particular, we impose a heat flux of the form $\bar{q} = \bar{q}_0 \exp(y - y_{\max})$, where y is

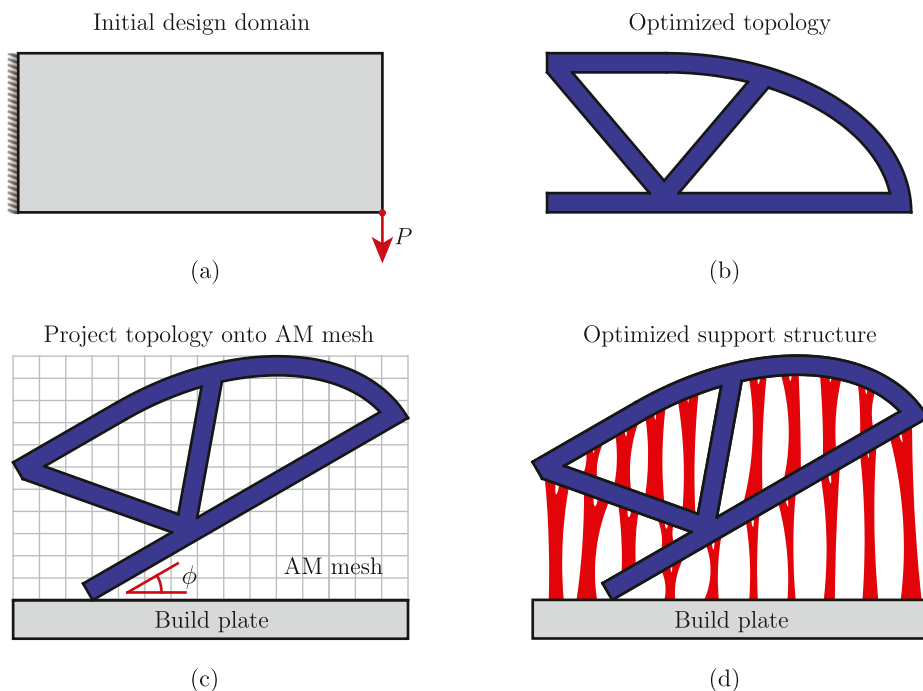


Fig. 4. Methodology for the design of support structures for additive manufacturing. Given an initial design domain (a), the topology optimization statement (1) is used to find the optimized topology of the primary structure (b). The primary structure is then projected onto a secondary mesh, called the additive manufacturing (AM) mesh (c), and then, the topology optimization statement (1) is used once more to design the support structure (d).

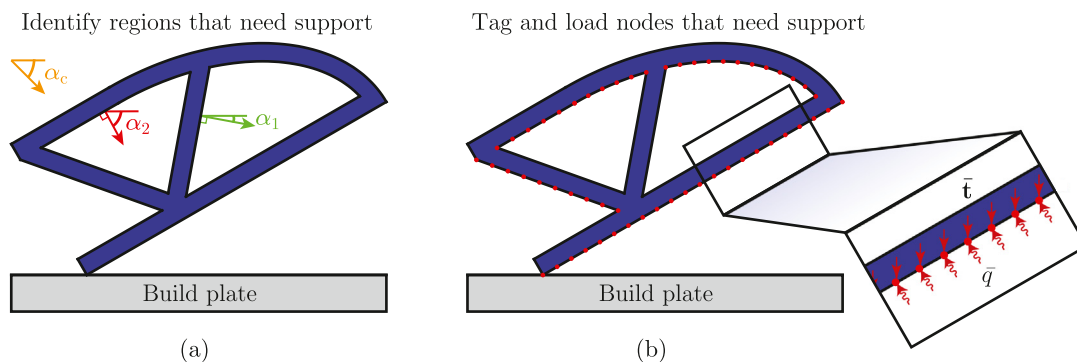


Fig. 5. Overhang detection process and thermomechanical loading conditions for the design of support structures: (a) an overhang detection algorithm is implemented to identify the regions of the primary structure that need to be supported; (b) the nodes from the AM mesh that need support material are tagged and then loaded with both a surface traction \bar{t} and a heat flux \bar{q} .

the height and y_{max} is the maximum height of the nodes that need support. The approach that we employ to design the support structures is meant to be an approximation, and thus, the thermomechanical loads that we impose are not necessarily accurate. However, as shown later, we are able to obtain reasonably sized support structures that could be useful in additive manufacturing.

The approach discussed above may lead to support structures with elements that are too thick to be easily removed after the part has been printed or to unsupported regions that are too large and may cause the part to fail during printing. To remedy these two issues, we control the maximum member size in the optimized topologies. By doing so, we obtain thinner elements that can be easily removed once the part has been printed and also obtain support structures with more elements, leading to better distribution of support for the part being printed.

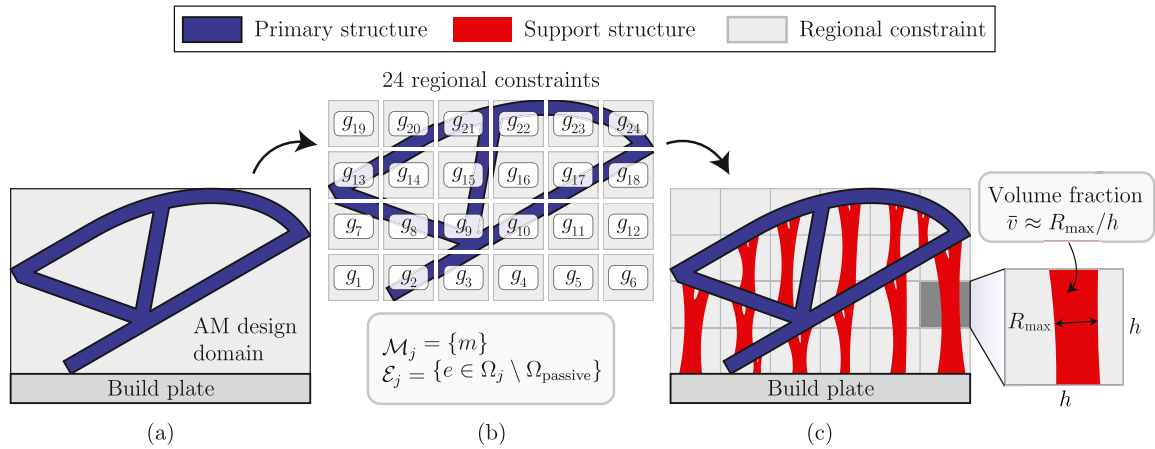


Fig. 6. Schematic illustration of regional volume constraints used to control the length scale of the support structures: (a) AM design domain; (b) 24 sub-regions used to define 24 regional constraints, each with volume fraction, \bar{v} ; and (c) a support structure with maximum member size, R_{max} , obtained using the regional constraints.

Traditionally, maximum member size is achieved by imposing a local constraint for each point in the design domain, such that members whose size is larger than a limit value are prevented (e.g., see [50,51]). These approaches lead to a prohibitively large number of constraints, which are typically clustered into a single constraint using a p -norm function. In the present work, we control the maximum member size by assigning multiple regional volume constraints, as discussed by Sanders et al. [10]. The number of regional constraints is, in general, much smaller than the number of elements (or nodes in the AM mesh), which leads to a reasonably low computational cost.

We determine the size of each regional constraint such that, for a given (prescribed) volume fraction, \bar{v} , we achieve a design with a desired maximum member size, R_{max} . If we assume that the regional constraints are squares of side h , the representative size of a regional constraint is given by

$$h = R_{max}/\bar{v}. \tag{38}$$

Given that the AM design domain is a rectangle of dimensions $B \times H$, the number of regional constraints, N_c , used to control the maximum member size is determined as

$$N_c = N_x N_y, \quad \text{where: } N_x = \left\lceil \frac{B}{h} \right\rceil \quad \text{and} \quad N_y = \left\lceil \frac{H}{h} \right\rceil, \tag{39}$$

where $\lceil x \rceil = \min\{n \in \mathbb{Z} \mid n \geq x\}$ is the ceiling function.

Fig. 6 provides a schematic illustration describing the way to control the length scale of the support structure via the regional volume constraints. The figure corresponds to a case in which 24 sub-regions are used to define 24 regional constraints (i.e., for $N = N_x N_y = 24$, with $N_x = 6$ and $N_y = 4$). We use Eq. (1)₂ to evaluate each constraint, g_j , and define the material indices as $\mathcal{M}_j = \{m\}$ and the element indices as $\mathcal{E}_j = \{e \in \Omega_j \setminus \Omega_{passive}\}$, in which m is the material index for the support structure, Ω_j are the element indices for sub-region j , and $\Omega_{passive}$ are the elements in the passive region.

Fig. 7 illustrates the effect of the number of regional constraints in the maximum member size of the support structures. As observed in the figure, as the number of regional constraints increases, the support structures become thinner (i.e., the maximum member size, R_{max} decreases) and more evenly distributed.

The time-dependent fabrication process is expected to affect the optimized layout of the support structures [52]. To obtain optimized support structures that account for the time-dependent fabrication process, one could employ the current approach in a layer-by-layer fashion, e.g., as discussed by Bruggi et al. [52], such that the state equations are solved on a space-time domain and the objective function is defined as an integral over time. Although feasible, the layer-by-layer approach is not explored in the present study.

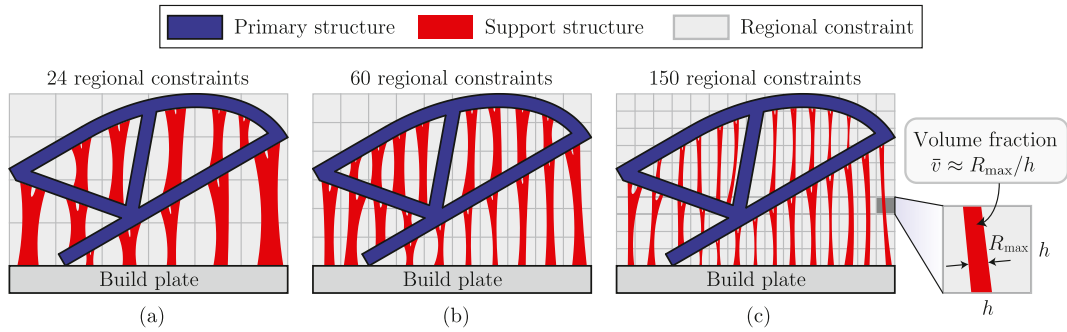


Fig. 7. Schematic plot illustrating the effect of the number of regional volume constraints, N_c , in the topology of the optimized support structures: (a) $N_c = 24$, (b) $N_c = 60$, and (c) $N_c = 150$. When N_c is the smallest, the support structures are bulky and difficult to remove, yet as N_c increases, the maximum member size R_{max} decreases and the resulting support structures become thinner and more evenly distributed.

Table 1

Numerical parameters used to solve all examples.

Parameter	Value
Ersatz parameter, ε_E	$1 \times 10^{-8} \min(E_i^0)$
Ersatz parameter, ε_β	$1 \times 10^{-8} \min(\beta_i^0)$
Ersatz parameter, ε_κ	$5 \times 10^{-3} \min(\kappa_i^0)$
Filter radius, R	0.015 m
Tolerance, Tol	0.001
Maximum number of iterations, MaxIter ^a	100
Move limit, move	0.1
Initial Hessian, $h_i^{\varepsilon,0}$	1×10^{-3}
Damping parameter, η	0.75

^aThis corresponds to the maximum number of iterations per continuation step.

6. Numerical results

In this section, we provide three numerical examples, which were solved using a Matlab implementation of the topology optimization formulation discussed previously. The examples illustrate several key aspects of the present formulation, including the versatility associated to the volume constraint setting, the ability to obtain smooth candidate Pareto fronts, the capability of designing support structures for additive manufacturing, among others. Unless otherwise specified, we use the parameters of Table 1 to obtain the results presented in this section.

6.1. Bridge design

This example illustrates the effects of different types of thermomechanical loads in the optimized topologies of a bridge-like structure obtained using our formulation. The geometry and thermomechanical loading conditions of the bridge, as well as the finite element discretization, are shown in Fig. 8. As depicted in Fig. 8a, a heat flux \bar{q} is applied on the deck and a body heat Q is applied in the entire design domain. The bridge is discretized with 75,000 polygonal finite elements using PolyMesher [53].

The bridge is made of three materials with thermomechanical properties shown in Fig. 9. The material properties have been arbitrarily selected such that material 1 is the stiffest but least conductive, material 3 is the most compliant but most conductive, and material 2 has intermediate stiffness and conductivity, but has the largest thermal stress coefficient. The arbitrariness with which the material properties have been selected is meant to show the capability of the formulation to select the best materials to achieve the best thermomechanical performance.

The geometry and loading conditions used to solve this problem are shown in Table 2. We consider two types of thermomechanical loads in the design. The first assumes $\bar{q} = 0.1 \text{ W/m}^2$ and $Q = 0$ and the second assumes $\bar{q} = 0$ and $Q = 1 \text{ W/m}^3$. For each of the two thermal loads, the bridge is subjected to a surface traction $\bar{t} = 5 \times 10^6 \text{ N/m}^2$. The first thermal load case ($\bar{q} = 0.1 \text{ W/m}^2$ and $Q = 0 \text{ W/m}^3$) may correspond to a case in which the bridge is

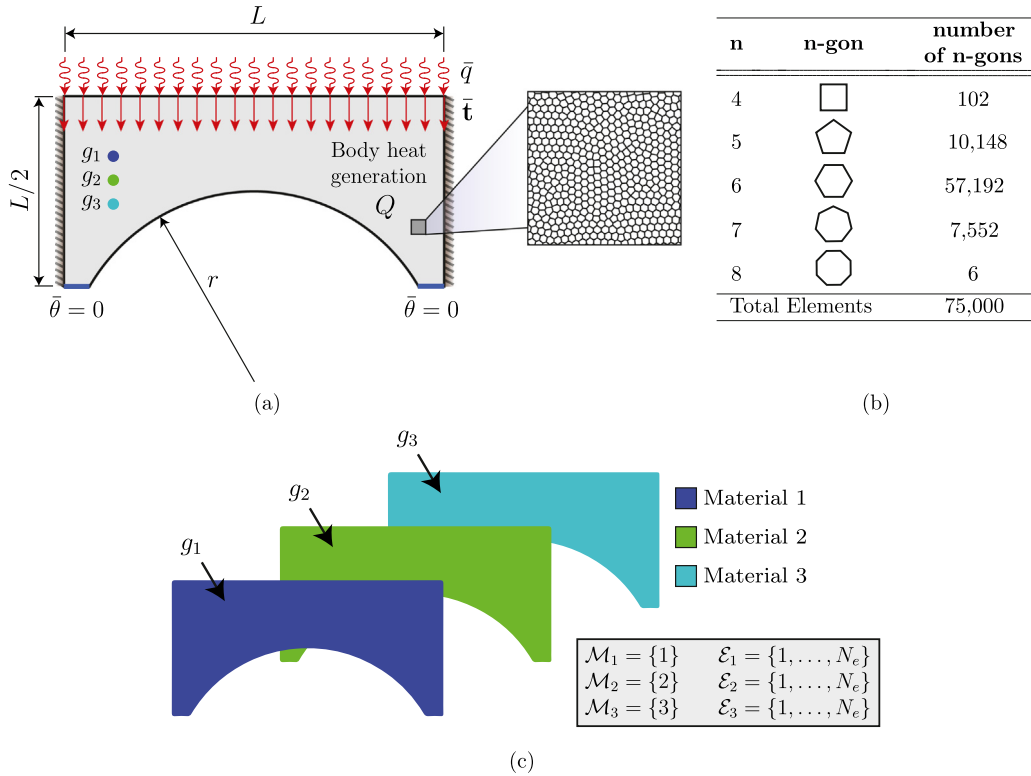


Fig. 8. Problem setup for the bridge design problem: (a) model geometry, loading, and boundary conditions; (b) mesh statistics; and (c) volume constraint setting comprising three constraints, each imposed to one of the candidate materials ($\mathcal{M}_j = \{j\}$, $j = 1, 2, 3$) and to all elements in the FE mesh ($\mathcal{E}_j = \{1, \dots, N_e\}$, $j = 1, 2, 3$).

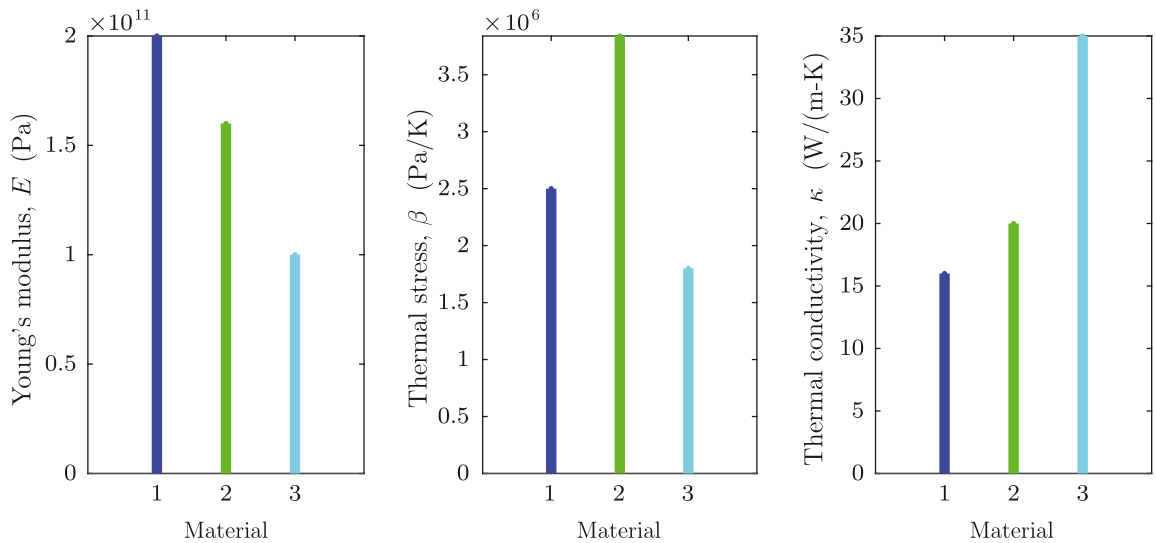


Fig. 9. Material properties for bridge structure.

subjected to solar radiation and the second ($\bar{q} = 0 \text{ W/m}^2$ and $Q = 1 \text{ W/m}^3$) to a case in which the bridge is

Table 2
Geometry and loading for the bridge design problem.

Parameter	Value
Bridge span, L	2 m
Radius, r	1 m
Center, y_c	-0.5 m
Surface load, \bar{t}	5×10^6 N/m ²
Heat flux, \bar{q}	0.1 W/m ² (or 0 W/m ²)
Body heat generation, Q	1 W/m ³ (or 0 W/m ³)

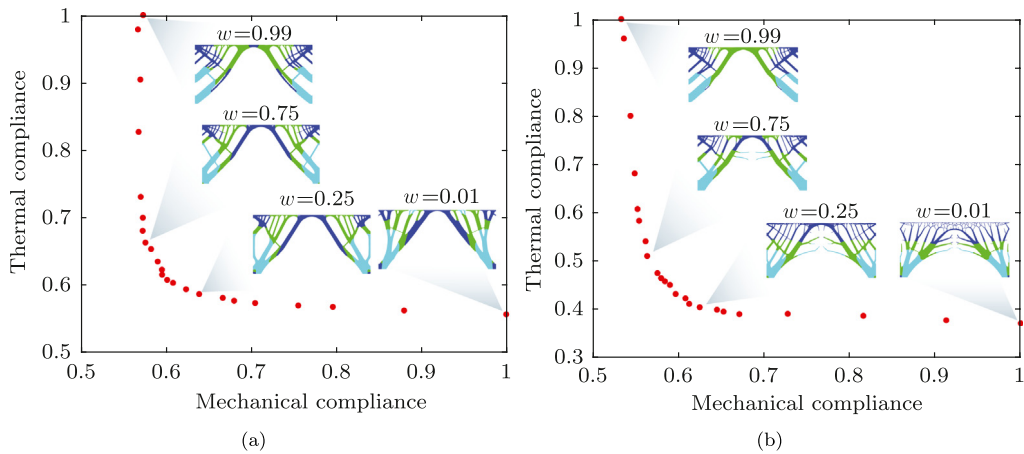


Fig. 10. Candidate Pareto fronts for bridge structure: (a) $\bar{q} = 0.1$ W/m², $Q = 0$ W/m³; and (b) $\bar{q} = 0$ W/m², $Q = 1$ W/m³.

subjected to body heat generated, e.g., from gas-based bridge heating systems [54]. Given that we use the present example for illustrative purposes, we have arbitrarily chosen the magnitude of thermal loads.¹

We use the approach described in Section 5.1 to construct one candidate Pareto front for each of the thermomechanical loads applied to the bridge and use thermal compliance (Eq. (6)) as the thermal objective function. The first candidate Pareto front, which corresponds to $\bar{q} = 0.1$ W/m² and $Q = 0$, is shown in Fig. 10a, and the second, which corresponds to $\bar{q} = 0$ and $Q = 1$ W/m³, is shown in Fig. 10b. Based on the two sets of results, it is clear that, as compared to the topologies obtained with body heat generation (Fig. 10b), those obtained with heat flux (Fig. 10a) contain less branches and thicker members. The branching observed in the results of Fig. 10b (when $w \rightarrow 0$) resemble tree-like structures, typically observed in the design of heat sinks (e.g., see [55,56]).

6.2. Flower design

In this example, we use the tangentially loaded donut-shaped domain shown in Fig. 11 to demonstrate how volume constraints can be specified to sub-regions of the design domain and how the multi-objective topology optimization can be used to obtain a multi-material topology while imposing only a global volume constraint in the entire design domain.² The information related to geometry and loading conditions for the donut-shaped domain of Fig. 11 are given in Table 3. We consider five candidate materials with thermomechanical properties shown in Fig. 12.

We solve two optimization problems, one with five regional volume constraints, each controlling one candidate material and defined in a sub-region of the design domain, and one with one global constraint controlling all

¹ For accurate values of the heat flux due to solar radiation, one could use the average energy flux from the sun on Earth, which is close to 350 W/m². Similarly, for accurate values of the body heat generation, one could use experimental measures on an actual bridge.

² In a linear elastic multi-material compliance minimization problem, imposing a global volume constraint controlling all candidate materials results in single-material topology composed of only the stiffest material [2,10].

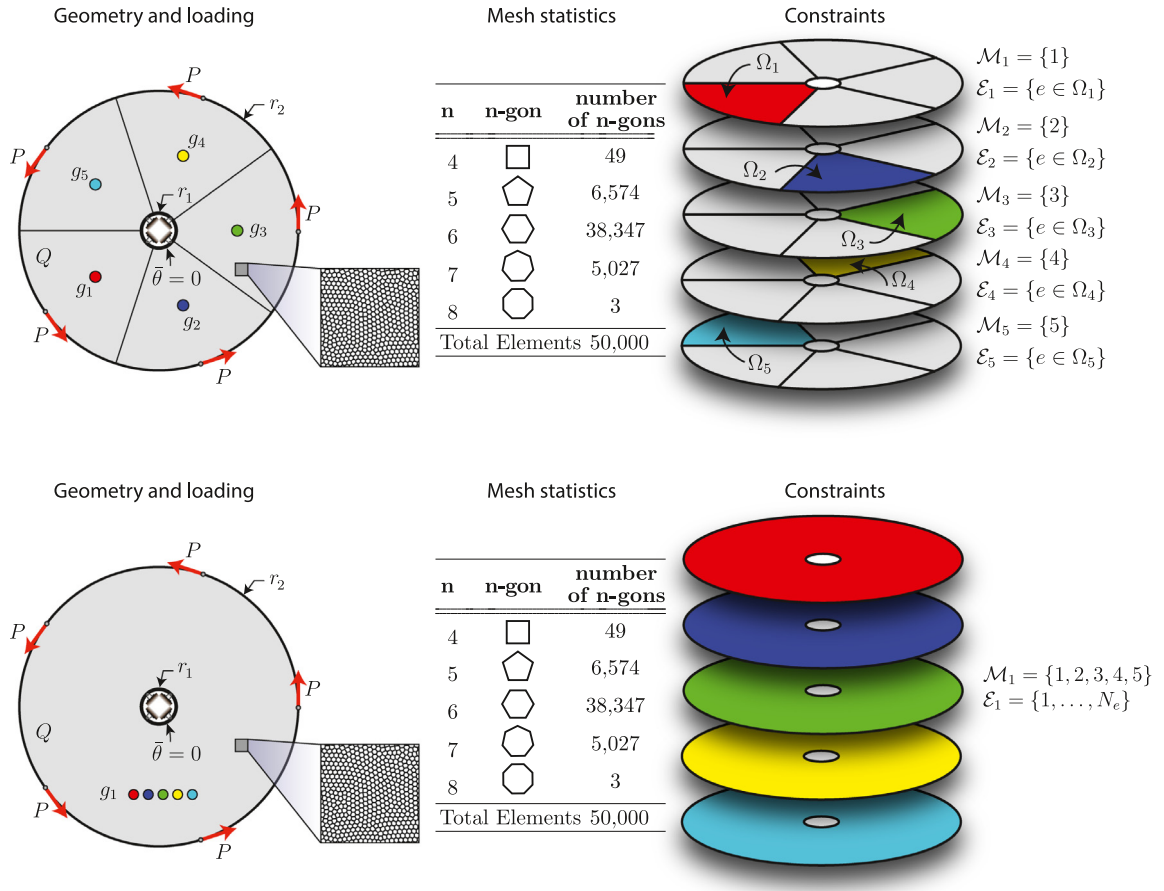


Fig. 11. Problem setup for the flower design problem with five regional constraints (top) and one global constraint (bottom): model geometry and loading (left), mesh statistics (middle), and volume constraint definition (right).

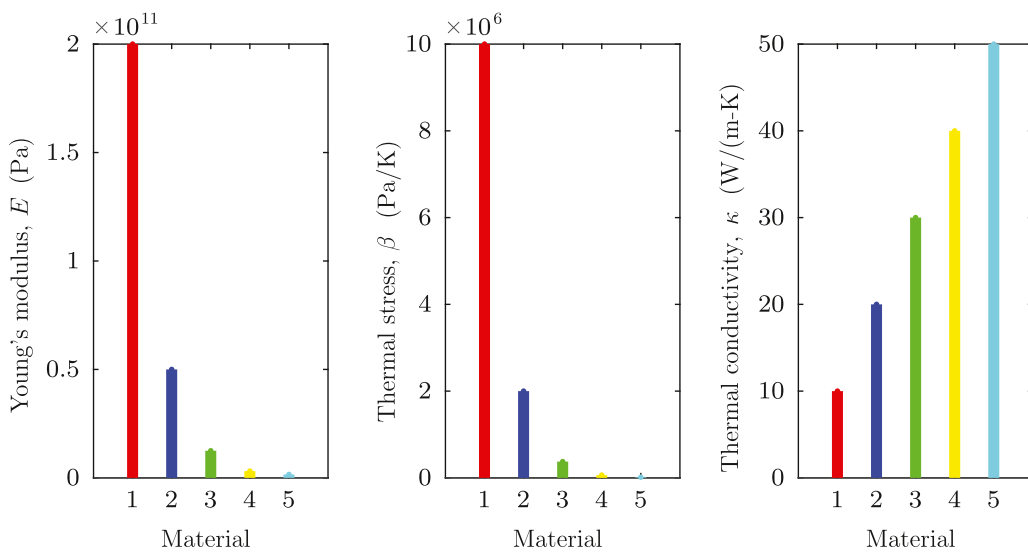


Fig. 12. Material properties for flower structure.

Table 3
Geometry and loading for the flower design problem.

Parameter	Value
Inner radius, r_1	0.125 m
Outer radius, r_2	1 m
Load, P	1×10^6 N
Body heat generation, Q	1 W/m ³

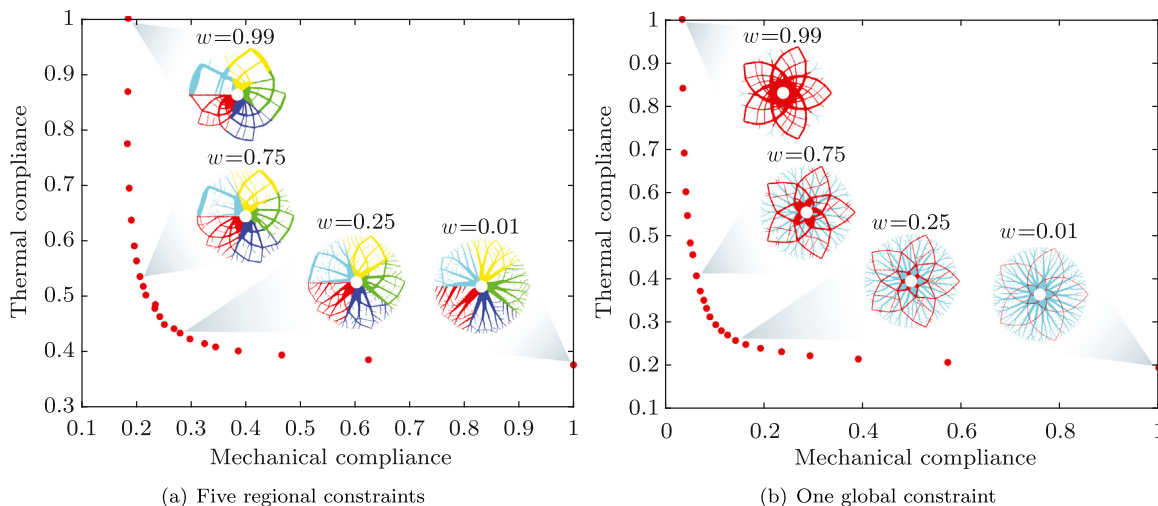


Fig. 13. Candidate Pareto fronts obtained using different volume constraint settings: (a) five regional constraints and (b) one global constraint.

candidate materials and defined in the entire design domain. We use Eq. (6) as the thermal objective function (i.e., thermal compliance) and obtain a candidate Pareto for each problem, as shown by the results in Fig. 13. The first candidate Pareto front (Fig. 13a) corresponds to the case in which five regional constraints are imposed, and the second (Fig. 13b) to the case in which a global volume constraint is imposed. Given that we impose one constraint per candidate material, the first candidate Pareto front is composed of five-material designs. As $w \rightarrow 1$, the optimized topologies resemble those obtained by Sanders et al. [10] for multi-material compliance minimization, and for values of $0 < w < 1$, the designs become a hybrid between a multi-material radial heat sink and the five-material flower by Sanders et al. [10].

For the second candidate Pareto front (Fig. 13b), we observe that, in contrast to single-physics topology optimization problems, our multi-physics formulation leads to multi-material topologies when a global volume constraint is imposed. According to the results, the optimized topologies obtained for intermediate values of w are composed of materials one and five, such that the stiffest material (material 1) is used to carry the applied loads and the more conductive material (material 5) is used to minimize the overall temperature of the structure. Thus, the optimizer is able to select the most appropriate material to achieve the best thermomechanical performance. The results also show that, as w increases, the amount of material one increases and that of material five decreases. That is because a larger value of w increases the relevance of the mechanical objective as compared to that of the thermal objective (see optimization statement (1)).

We also study the effect of the choice of thermal objective function in the optimized topologies obtained using our thermomechanical formulation. For the case in which five regional constraints are imposed, we use $w = 0.5$ and obtain the optimized topology either using thermal compliance (Eq. (6)) or using temperature variance (Eq. (7)) as thermal objective functions, J_θ , in (1). The optimization results are displayed in Fig. 14. The topologies obtained for each of the thermal objective functions are different and they lead to significantly different temperature distributions. First, note that the topology obtained for the thermal compliance case (Fig. 14a) have less small-scale features than that obtained for the temperature variance case (Fig. 14b). By having more small-scale features, the structure designed for thermal variance has a more homogeneous temperature distribution than that for the thermal compliance

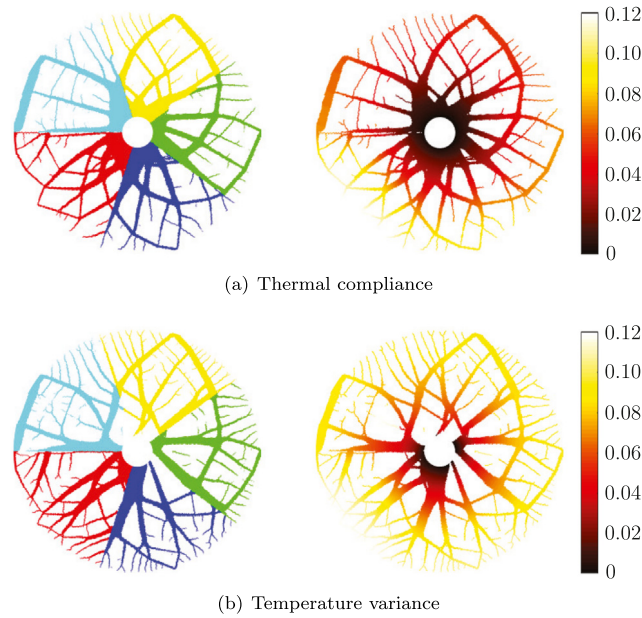


Fig. 14. Optimized topologies (left) and temperature distribution (right) obtained using (a) thermal compliance and (b) temperature variance.

Table 4
Geometry and loading for the antenna bracket design problem.

Parameter	Value
Length, L	1 m
Height, H	1.75 m
Radius, r	0.66 m
Load, P	5×10^6 N
Moment, M	3.12×10^6 N m

case. The results also show that, in the thermal compliance case, the five materials are fully connected to the inner circle (the heat sink), thus helping to reduce the overall temperature of the structure. However, for the temperature variance case, all materials are not fully connected to the heat sink, which in turn leads to a more homogeneous temperature distribution. As a result, it is expected that the designs obtained using temperature variance experience less thermal warping than those obtained using thermal compliance.

6.3. Antenna support bracket design

The last example aims to design the support structure for the additive manufacturing of a topology optimized antenna support bracket. We use the procedure described in Section 5.2 to obtain the topology of both the bracket and the support structure. For the design of the bracket, we use the problem setup shown in Fig. 15. The geometry and loading conditions for the bracket are given in Table 4. The antenna is loaded with a vertical load of magnitude $P = 5 \times 10^6$ N and a moment of magnitude $M = 3.12 \times 10^6$ N m (Fig. 15a). The design domain is discretized using 50,000 polygonal elements, as shown in Fig. 15a–b. As depicted in Fig. 15c, we consider three candidate materials and impose one volume constraint to each of them. We then solve the optimization statement (1) using $w = 1$ and obtain the optimized topology shown in Fig. 15d.

After obtaining the optimized topology of the bracket, we use the optimization statement (1) once more to design the support structure. The support structures are designed considering J_θ based on thermal compliance. For this purpose, we follow the procedure discussed in Section 5.2 and project the optimized topology onto a second

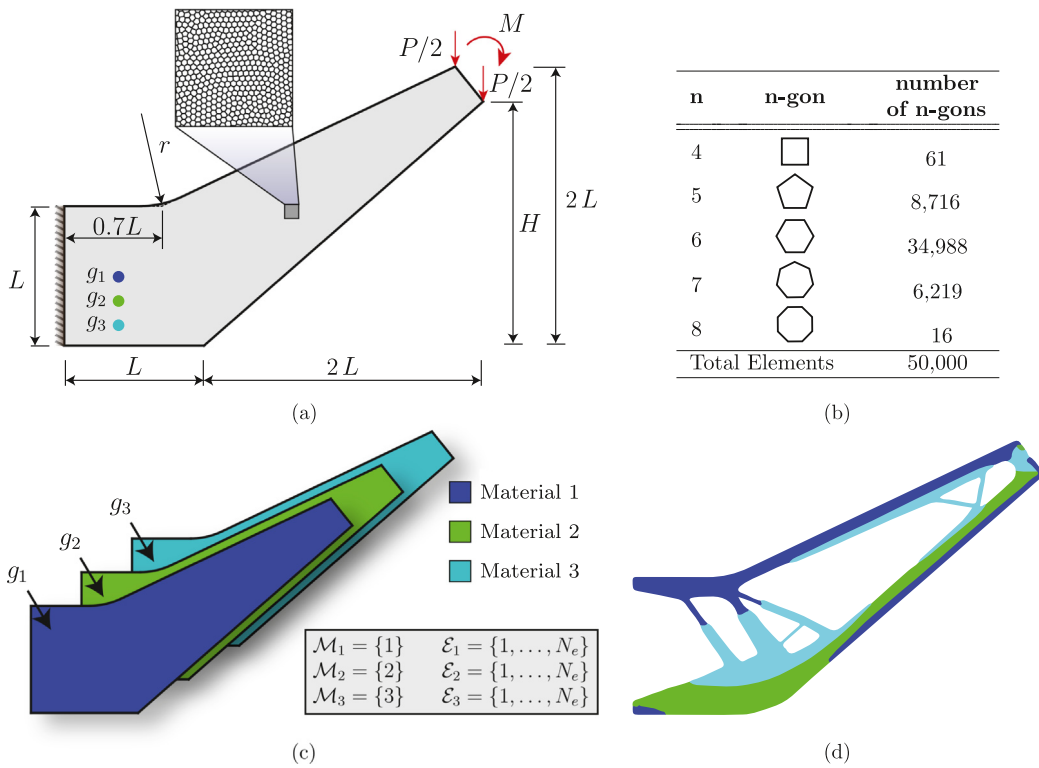


Fig. 15. Design of an antenna support bracket: (a) design domain, loading, and boundary conditions; (b) distribution of polygonal elements in the FE mesh; (c) volume constraint setting; and (d) optimized topology.

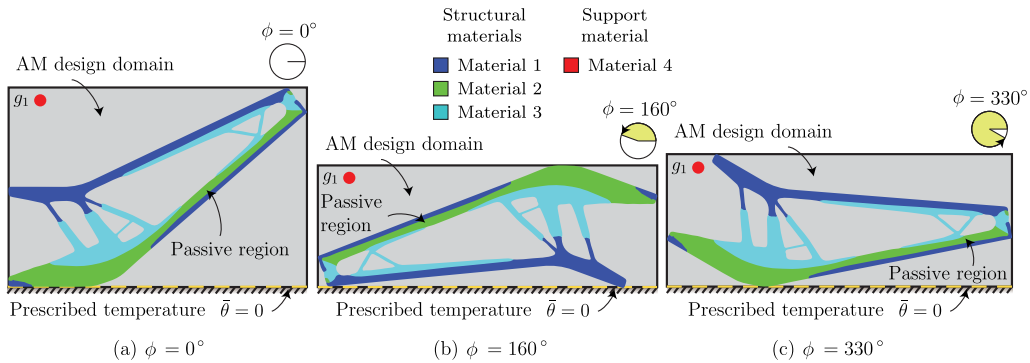


Fig. 16. Problem setting for the design of the support structure for the antenna support bracket for different print orientations, ϕ . In the current setup, we add a fourth material, which we use for the design of the support structure.

mesh (the AM mesh), which we use to solve a new problem with different thermal and mechanical loads used for the design of the support structure. As shown in Fig. 16, we consider three different print orientations, ϕ , which lead to three different AM design domains, and thus, to three different AM meshes. For the design of the support structure, we have added a fourth material (material 4), which is used as the support material.

We use the optimization statement (1) with $w = 0.5$ to obtain the optimized topology of the support structure for each of the three print orientations discussed previously. The topologies of the support structures are shown

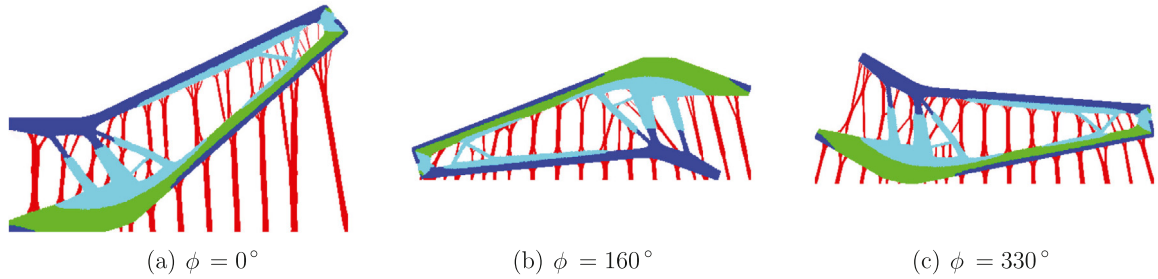


Fig. 17. Effect of print orientation, ϕ , in the optimized topology of the support structure.

		Maximum member size, R_{\max}		
		0.025	0.050	0.100
Volume fraction, \bar{v}	0.2			
	0.3			
	0.4			

Fig. 18. Effect of maximum member size, R_{\max} , and volume fraction, \bar{v} , in the optimized topology of the support structure for a print orientation $\phi = 160^\circ$.

in Fig. 17. To obtain these designs, we consider a maximum member size of $R_{\max} = 0.05$ and a volume fraction $\bar{v} = 0.3$. As shown in the figure, the amount of support material for $\phi = 0^\circ$ is larger than that required for $\phi = 160^\circ$ and $\phi = 330^\circ$.

An interesting feature of the support structures obtained with our formulation is the branched-type connection between the support material and the primary structure. The branching helps both to absorb heat from the primary structure and to give a more uniform support to the structure in order to minimize displacements. The branching obtained in the contact regions facilitates the removal of the support material after the structure is printed, which reduces manufacturing costs.

Depending on the printer used, the spacing between members in the support structures shown in Fig. 17 may be inadequate and the prints may fail. We can control the spacing between members in the support structure by varying the maximum member size, R_{\max} , and the volume fraction, \bar{v} , which can lead to a more evenly distributed support structure. We investigate the effects of these two parameters in the optimized topologies of the support structures and show the results in Fig. 18 for $\phi = 160^\circ$ and in Fig. 19 for $\phi = 330^\circ$. From the results, we observe that, as the maximum member size decreases, the number of members in the optimized support structures increases and the spacing between members decreases. The results also show that increasing the volume fraction generally leads to support structures with an increasing number of members.

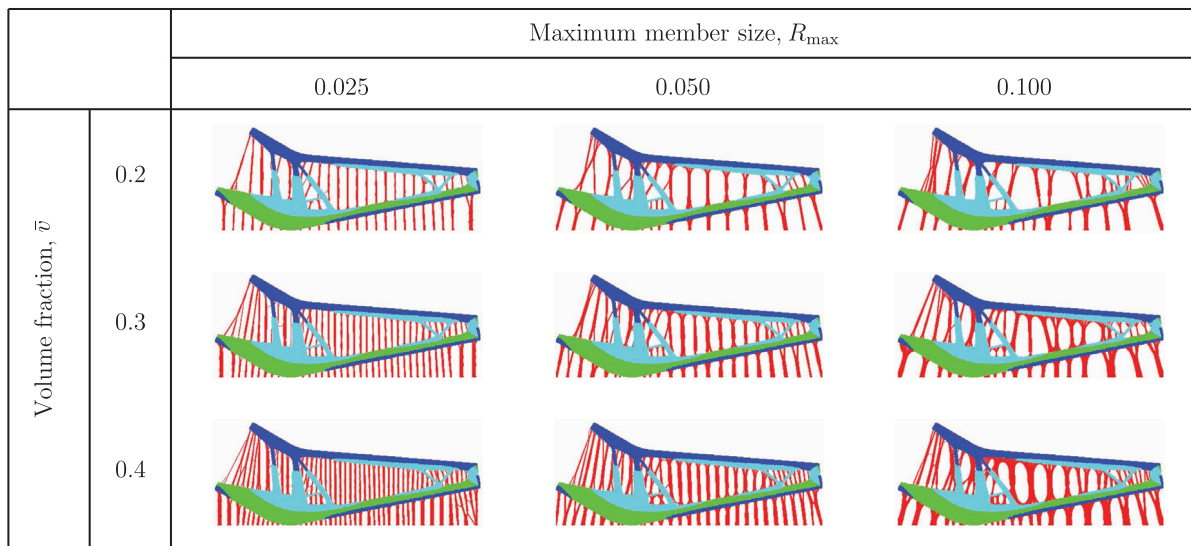


Fig. 19. Effect of maximum member size, R_{\max} , and volume fraction, \bar{v} , in the optimized topology of the support structure for a print orientation $\phi = 330^\circ$.

7. Assessment of computational efficiency

Here, we investigate the computational efficiency of the proposed formulation using some of the results from the examples of the previous section.³ From example 2, we determine the computational cost required to obtain one point of the candidate Pareto front both for the case of one global volume constraint for that of five regional constraints. Similarly, from example 3, we determine the computational cost required to obtain the topology of the support structures for a print orientation $\phi = 160^\circ$ and for a volume fraction of $\bar{v} = 0.3$ (i.e., for the middle row in Fig. 18). We also compare the computational cost obtained using the present formulation with that obtained using MMA.

The computational cost required to obtain one point of the candidate Pareto front of Example 2 is shown in Fig. 20. The results show that, independently of the number of constraints, N_c , the time used by MMA to update the design variables is much larger than that required by our sensitivity separation approach. The difference between the two methods is particularly notorious when $N_c = 1$, in which MMA takes about 14 min to update the design variables (i.e., about 38% of the total time), but our sensitivity separation method takes less than 1 min (i.e., about 3% of the total time). We also observe that, when compared to the case in which $N_c = 1$ (Fig. 20a), the computational cost used to update the design variables is smaller when $N_c = 5$ (Fig. 20b). The computational cost reduces because the dual problems that need to be solved to obtain the Lagrange multipliers for $N_c = 5$ are smaller than the dual problem that needs to be solved to find the Lagrange multiplier for $N_c = 1$.

We also report the computational time for the design of the support structure of the antenna support bracket shown in the last example of the previous section. The breakdown of computational times is reported in Fig. 21. As R_{\max} decreases, the number of volume constraints, N_c , increases (see Eq. (39)), and thus the overall computational time also increases. The increase in computational cost as R_{\max} decreases is mainly due to the increase in computational cost of the sensitivity computation of the volume constraints. For example, when $R_{\max} = 0.025$, the model has 538 constraints, which considerably increases the cost of sensitivity evaluation. One way to increase the performance of constraint sensitivity evaluation is to perform the computations in parallel, yet such extension is out of the scope of the present study.

³ Here, the computational efficiency is assessed by measuring the CPU time required to obtain the optimized topologies. The examples from the previous section were run using Matlab R2017b on a desktop computer with an Intel(R) Xenon(R) CPU E5-1660 v3 at 3.00 GHz and 256 GB of RAM running on a 64-bit operating system.

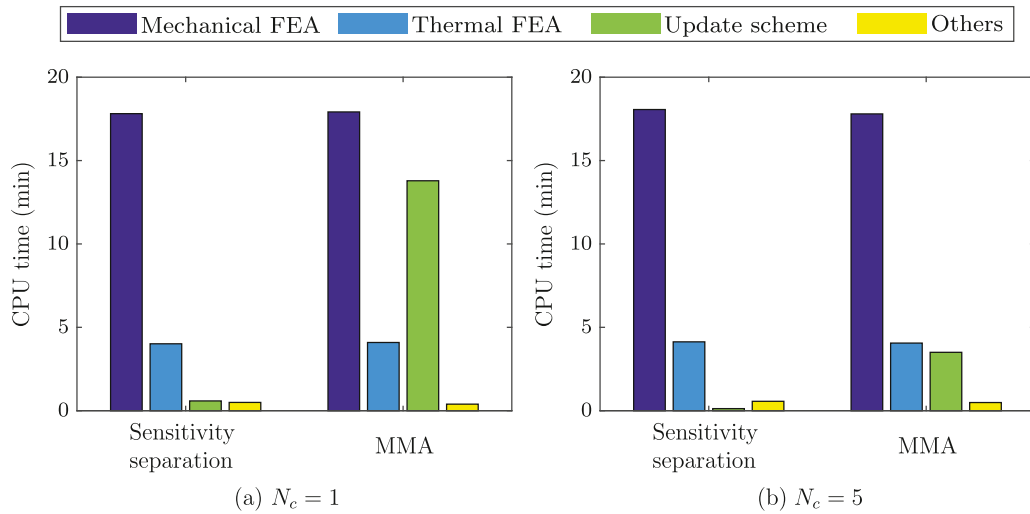


Fig. 20. Distribution computational time required to obtain one point of each of the candidate Pareto fronts shown in Fig. 13: (a) results for $N_c = 1$ and (b) results for $N_c = 5$. The results obtained using the design variable update scheme based on sensitivity separation are compared against those obtained using MMA.

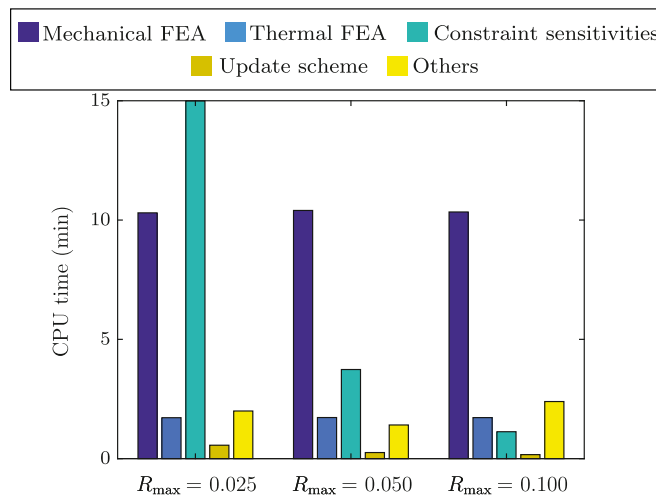


Fig. 21. Distribution computational time for the design of the support structure for an antenna support bracket. The computational times are reported for a volume fraction of $\bar{v} = 0.3$ and for various values of the maximum member size, R_{max} . The number of volume constraints increases as R_{max} decreases, causing the overall computational to also increase.

8. Concluding remarks

We have presented a formulation for the topology optimization of multi-material thermoelastic structures. The formulation has been developed as a multi-objective topology optimization problem that considers both a mechanical objective function and a thermal objective function. By taking advantage of the generality of the ZPR design variable update scheme [1], we have developed a design variable update scheme that is capable of solving non-self-adjoint topology problems in an efficient way. Similarly to the ZPR design variable update scheme, our scheme can update the design variables for each volume constraint independently. The numerical results show that our design variable update scheme is considerably faster than MMA.

We use the formulation to construct smooth candidate Pareto fronts, which is possible due to the continuation scheme introduced by Sanders et al. [10] for multi-material continuum topology optimization. In addition, we use the

formulation to design support structures for additive manufacturing. By varying the volume fraction of the support material and the maximum member size of the support structure, we are able to achieve designs that provide a continuous support for the structure to be printed.

Acknowledgments

We acknowledge the financial support by Siemens, USA Corporate Technology for the project “Multi-material Topology Optimization with Arbitrary Volume Constraints – A Multi-physics Approach” and endowment provided by the Raymond Allen Jones Chair at the Georgia Institute of Technology. We also thank Mr. Fernando V. da Senhora for useful discussions, which helped improving both the formulation and the manuscript. The information presented in this paper is the sole opinion of the authors and does not necessarily reflect the views of the sponsors or sponsoring agencies.

Appendix. Nomenclature

E_e	Effective Young’s modulus for element e
J	Objective function
J_m	Mechanical objective function
J_θ	Thermal objective function
N_c	Number of volume constraints
N_e	Number of elements in the FE mesh
N_n	Number of nodes in the FE mesh
Q	Body heat generation
R_{\max}	Maximum member size
\bar{q}	Heat flux prescribed on boundary Γ_q
\bar{v}_j	Volume fraction limit for constraint j
\tilde{J}	Non-monotonous convex approximation of the objective function
g_j	j th volume constraint
m	Number of candidate materials
p	SIMP penalty coefficient
R	Filter radius
v_e	Area of element e
w	Weight factor
\mathcal{E}_j	Set of element indices for constraint j
\mathcal{M}_j	Set of material indices for constraint j
$\partial J^+ / \partial z_i^e$ and $\partial J^- / \partial z_i^e$	Positive and negative sensitivity components in sensitivity separation approach
$\bar{\theta}$	Temperature prescribed on boundary Γ_θ
β_e	Effective thermal stress coefficient for element e
γ	Mixing penalty parameter
κ_e	Effective thermal conductivity for element e
ϕ	Print orientation
θ_e	Temperature change evaluated at the centroid of element e
θ_{avg}	Average temperature change in the design domain
H	Conductivity matrix
K	Stiffness matrix
P	Filter matrix
$\mathbf{a}_i, \mathbf{b}_i$	Parameters used to define the convex approximation of the objective function
\mathbf{f}_m	External force vector
\mathbf{f}_θ	Thermal flux vector for thermal FE problem
\mathbf{f}_{th}	Thermal force vector for mechanical FE problem
h	Approximation of the diagonal of the Hessian matrix

\mathbf{q}	Heat flux vector
\mathbf{u}	Displacement vector
$\mathbf{z}_1, \dots, \mathbf{z}_m$	Vectors of design variables for candidate material, $i = 1, \dots, m$
ρ_1, \dots, ρ_m	Vectors of filtered densities for candidate material, $i = 1, \dots, m$
θ	Nodal temperature vector

References

- [1] X. Zhang, G.H. Paulino, A.S. Ramos Jr., Multi-material topology optimization with multiple volume constraints: A general approach applied to ground structures with material nonlinearity, *Struct. Multidiscip. Optim.* 57 (1) (2018) 161–182, <http://dx.doi.org/10.1007/s00158-017-1768-3>.
- [2] E.D. Sanders, M.A. Aguiló, G.H. Paulino, Multi-material continuum topology optimization with arbitrary volume and mass constraints, *Comput. Methods Appl. Mech. Engrg.* 340 (2018) 798–823.
- [3] Y. Jiang, A.S. Ramos Jr., G.H. Paulino, Topology optimization with design-dependent loading: An adaptive sensitivity-separation design variable update scheme, *Struct. Multidiscip. Optim.* (2020) <http://dx.doi.org/10.1007/s00158-019-02430-4>, in press.
- [4] K.V. Wong, A. Hernandez, A review of additive manufacturing, *ISRN Mech. Eng.* 2012 (2012) 1–10.
- [5] I. Gibson, D. Rosen, B. Stucker, *Additive Manufacturing Technologies: 3D Printing, Rapid Prototyping, and Direct Digital Manufacturing*, Vol. 2, Springer, 2015.
- [6] T. Zegard, G.H. Paulino, Bridging topology optimization and additive manufacturing, *Struct. Multidiscip. Optim.* 53 (1) (2016) 175–192.
- [7] J. Qi, J. Halloran, Negative thermal expansion artificial material from iron-nickel alloys by oxide co-extrusion with reductive sintering, *J. Mater. Sci.* 39 (13) (2004) 4113–4118.
- [8] A.T. Gaynor, N.A. Meisel, C.B. Williams, J.K. Guest, Multiple-material topology optimization of compliant mechanisms created via PolyJet three-dimensional printing, *J. Manuf. Sci. Eng.* 136 (6) (2014) 061015.
- [9] C. Schumacher, B. Bickel, J. Rys, S. Marschner, C. Daraio, M. Gross, Microstructures to control elasticity in 3D printing, *ACM Trans. Graph.* 34 (4) (2015) 136.
- [10] E.D. Sanders, A. Pereira, M.A. Aguiló, G.H. Paulino, PolyMat: an efficient Matlab code for multi-material topology optimization, *Struct. Multidiscip. Optim.* 58 (6) (2018) 2727–2759.
- [11] H. Rodrigues, P. Fernandes, A material based model for topology optimization of thermoelastic structures, *Internat. J. Numer. Methods Engrg.* 38 (12) (1995) 1951–1965.
- [12] O. Sigmund, Design of multiphysics actuators using topology optimization—Part I: One-material structures, *Comput. Methods Appl. Mech. Engrg.* 190 (49–50) (2001) 6577–6604.
- [13] O. Sigmund, Design of multiphysics actuators using topology optimization—Part II: Two-material structures, *Comput. Methods Appl. Mech. Engrg.* 190 (9) (2001) 6605–6627.
- [14] Y. Du, Z. Luo, Q. Tian, L. Chen, Topology optimization for thermo-mechanical compliant actuators using mesh-free methods, *Eng. Optim.* 41 (8) (2009) 753–772.
- [15] O. Sigmund, S. Torquato, Composites with extremal thermal expansion coefficients, *Appl. Phys. Lett.* 69 (21) (1996) 3203–3205.
- [16] O. Sigmund, S. Torquato, Design of materials with extreme thermal expansion using a three-phase topology optimization method, *J. Mech. Phys. Solids* 45 (6) (1997) 1037–1067.
- [17] N. de Kruijf, S. Zhou, Q. Li, Y. Mai, Topological design of structures and composite materials with multiobjectives, *Int. J. Solids Struct.* 44 (22–23) (2007) 7092–7109.
- [18] A. Faure, G. Michailidis, G. Parry, N. Vermaak, R. Estevez, Design of thermoelastic multi-material structures with graded interfaces using topology optimization, *Struct. Multidiscip. Optim.* 56 (4) (2017) 823–837.
- [19] Q. Xia, M. Wang, Topology optimization of thermoelastic structures using level set method, *Comput. Mech.* 42 (6) (2008) 837–857.
- [20] Q. Li, G.P. Steven, Y.M. Xie, Displacement minimization of thermoelastic structures by evolutionary thickness design, *Comput. Methods Appl. Mech. Engrg.* 179 (3–4) (1999) 361–378.
- [21] Q. Li, G. Steven, Y. Xie, Thermoelastic topology optimization for problems with varying temperature fields, *J. Therm. Stresses* 24 (4) (2001) 347–366.
- [22] Q. Li, G. Steven, Y. Xie, O. Querin, Evolutionary topology optimization for temperature reduction of heat conducting fields, *Int. J. Heat Mass Transfer* 47 (23) (2004) 5071–5083.
- [23] A. Takezawa, G. Yoon, S. Jeong, M. Kobashi, M. Kitamura, Structural topology optimization with strength and heat conduction constraints, *Comput. Methods Appl. Mech. Engrg.* 276 (2014) 341–361.
- [24] J. Deaton, R. Grandhi, Stress-based design of thermal structures via topology optimization, *Struct. Multidiscip. Optim.* 53 (2) (2016) 253–270.
- [25] S. Deng, K. Suresh, Stress constrained thermo-elastic topology optimization with varying temperature fields via augmented topological sensitivity based level-set, *Struct. Multidiscip. Optim.* 56 (6) (2017) 1413–1427.
- [26] J. Yan, G. Cheng, L. Liu, A uniform optimum material based model for concurrent optimization of thermoelastic structures and materials, *Int. J. Simul. Multidiscip. Des. Optim.* 2 (4) (2008) 259–266.
- [27] J. Yan, X. Guo, G. Cheng, Multi-scale concurrent material and structural design under mechanical and thermal loads, *Comput. Mech.* 57 (3) (2016) 437–446.
- [28] L. Liu, J. Yan, G. Cheng, Optimum structure with homogeneous optimum truss-like material, *Comput. Struct.* 86 (13–14) (2008) 1417–1425.

- [29] J. Deng, J. Yan, G. Cheng, Multi-objective concurrent topology optimization of thermoelastic structures composed of homogeneous porous material, *Struct. Multidiscip. Optim.* 47 (4) (2013) 583–597.
- [30] T. Gao, W. Zhang, Topology optimization involving thermo-elastic stress loads, *Struct. Multidiscip. Optim.* 42 (5) (2010) 725–738.
- [31] J. Stegmann, E. Lund, Discrete material optimization of general composite shell structures, *Internat. J. Numer. Methods Engrg.* 62 (14) (2005) 2009–2027.
- [32] E. Lund, J. Stegmann, On structural optimization of composite shell structures using a discrete constitutive parametrization, *Wind Energy* 8 (2005) 109–124.
- [33] T. Gao, P. Xu, W. Zhang, Topology optimization of thermo-elastic structures with multiple materials under mass constraint, *Comput. Struct.* 173 (2016) 150–160.
- [34] G. Allaire, B. Bogossel, Optimizing supports for additive manufacturing, *Struct. Multidiscip. Optim.* 58 (6) (2018) 2493–2515.
- [35] G. Allaire, C. Dapogny, R. Estevez, A. Faure, G. Michailidis, Structural optimization under overhang constraints imposed by additive manufacturing technologies, *J. Comput. Phys.* 351 (2017) 295–328.
- [36] A.M. Mirzendehtel, K. Suresh, Support structure constrained topology optimization for additive manufacturing, *Computer-Aided Design* 81 (2016) 1–13.
- [37] B. Bourdin, Filters in topology optimization, *Internat. J. Numer. Methods Engrg.* 50 (9) (2001) 2143–2158.
- [38] M.P. Bendsøe, Optimal shape design as a material distribution problem, *Struct. Optim.* 1 (1989) 193–202.
- [39] M.P. Bendsøe, O. Sigmund, Material interpolation schemes in topology optimization, *Arch. Appl. Mech.* 69 (9–10) (1999) 635–654.
- [40] C. Fleury, CONLIN: An efficient dual optimizer based on convex approximation concepts, *Struct. Optim.* 1 (2) (1989) 81–89.
- [41] C. Fleury, V. Braibant, Structural optimization: A new dual method using mixed variables, *Internat. J. Numer. Methods Engrg.* 23 (3) (1986) 409–428.
- [42] K. Svanberg, The method of moving asymptotes—A new method for structural optimization, *Internat. J. Numer. Methods Engrg.* 24 (2) (1987) 359–373.
- [43] P. Duysinx, W. Zhang, C. Fleury, V.H. Nguyen, S. Haubruge, A new separable approximation scheme for topological problems and optimization problems characterized by a large number of design variables, in: *Proceedings of the First World Congress of Structural and Multidisciplinary Optimization (WCSMO1)*, 1995, pp. 1–8.
- [44] C.G. Broyden, The convergence of a class of double-rank minimization algorithms I. General considerations, *IMA J. Appl. Math.* 6 (1) (1970) 76–90.
- [45] R. Fletcher, A new approach to variable metric algorithms, *Comput. J.* 13 (3) (1970) 317–322.
- [46] D. Goldfarb, A family of variable-metric methods derived by variational means, *Math. Comp.* 24 (109) (1970) 23–26.
- [47] D.F. Shanno, Conditioning of quasi-Newton methods for function minimization, *Math. Comp.* 24 (111) (1970) 647–656.
- [48] M.P. Bendsøe, *Optimization of Structural Topology, Shape, and Material*, Vol. 414, Springer, 1995.
- [49] A.A. Groenwold, L.F.P. Etman, On the equivalence of optimality criterion and sequential approximate optimization methods in the classical topology layout problem, *Internat. J. Numer. Methods Engrg.* 73 (3) (2008) 297–316.
- [50] J.K. Guest, Imposing maximum length scale in topology optimization, *Struct. Multidiscip. Optim.* 37 (5) (2009) 463–473.
- [51] E. Fernández, M. Collet, S. Bauduin, E. Lemaire, P. Duysinx, Contributions to handle maximum size constraints in density-based topology optimization, in: *Proceedings of the 12th World Congress of Structural and Multidisciplinary Optimization (WCSMO12)*, Springer, 2017, pp. 1054–1068.
- [52] M. Bruggi, N. Parolini, F. Regazzoni, M. Verani, Topology optimization with a time-integral cost functional, *Finite Elem. Anal. Des.* 140 (2018) 11–22.
- [53] C. Talischí, G.H. Paulino, A. Pereira, I.F.M. Menezes, *PolyMesher*: a general-purpose mesh generator for polygonal elements written in Matlab, *Struct. Multidiscip. Optim.* 45 (3) (2012) 309–328.
- [54] W.J. Eugster, Road and bridge heating using geothermal energy. Overview and examples, in: *Proceedings of the European Geothermal Congress 2007*, Unterhaching, Germany, 2007, pp. 1–5.
- [55] A. Gersborg-Hansen, M. Bendsøe, O. Sigmund, Topology optimization of heat conduction problems using the finite volume method, *Struct. Multidiscip. Optim.* 31 (4) (2006) 251–259.
- [56] J. Alexandersen, O. Sigmund, N. Aage, Large scale three-dimensional topology optimisation of heat sinks cooled by natural convection, *Int. J. Heat Mass Transfer* 100 (2016) 876–891.